

## Earth Sciences and Environmental Technologies Division

<b>Study</b>	MPN12	<b>Division chrono</b>	<i>RXXX/n° YY-XXXX</i>
<b>Partners</b>		<b>Contract</b>	1997C0022

<b>Title</b>	<b>Assuring integrity of CO<sub>2</sub> storage sites through ground surface monitoring (SENSE) - WP2.3: Numerical simulation of ground movement in response to reservoir pressure change for the candidate sites (Deliverable D2.3)</b>		
<b>Author(s) and membership</b>	BOUQUET Sarah, BRUCH Andre, FREY Jeremy, CACAS Marie-Christine		
<b>Diffusion</b>	Public	<b>Publication date</b>	<i>m/d/yyyy</i>
<b>Division visa</b> <i>Scientific authentication</i>	ROGGERO Frederic	<b>Project visa</b> <i>Specification compliance</i>	ROGGERO Frederic

<b>Keywords</b>	Surface displacement – Coupled flow-geomechanical simulation – CO <sub>2</sub> storage integrity – Dual-Medium – CO <sub>2</sub> leakage
-----------------	--

<b>Summary</b>
<p>The project, SENSE, is funded through the ACT program (Accelerating CCS Technologies, Horizon2020 Project No 294766). Its objective is to demonstrate how surface displacements can be used in a monitoring program aimed at verifying the long-term integrity of a CO<sub>2</sub> geological storage site. IFPEN participates as WP2 (work package) leader to coordinate 3D coupled hydromechanical simulation activities to understand the surface displacement mechanism in response to pressure changes due to CO<sub>2</sub> injection. This report addresses the Task 2.3: Numerical simulation of ground movement in response to reservoir pressure change for the candidate sites.</p> <p>We address the specificities encountered at the considered real site, In Salah: development of an effective dual-medium hydromechanical coupling and conceptual CO<sub>2</sub> leakage scenario with a surface displacement footprint comparable to the one from In Salah. In addition, we also produce a preliminary study of the possible thermal effect(s) of cold CO<sub>2</sub> injection on subsurface mechanical behavior.</p> <p>The coupled hydromechanical simulations for the In Salah model calibration, based on InSAR data and relevant information related to this CO<sub>2</sub> storage site are presented in deliverable 3.2.</p>

## Earth Sciences and Environmental Technologies Division

Diffusion list (pdf)	E-mail address
HUYGHE Raphael	
SOUQUE Christine	
ESNAULT Vivien	
GERVAIS-COUPLET Véronique	
VINCKE Olivier	
ESTUBLIER Audrey	
ALAVOINE Axelle	
BOHLOLI Bahman (NGI)	<a href="mailto:Bahman.Bohloli@ngi.no">Bahman.Bohloli@ngi.no</a>
TOMA Oksana (ADEME)	<a href="mailto:Oksana.toma@ademe.fr">Oksana.toma@ademe.fr</a>
DOUARCHE Frédéric	

For agreement,

### Table of contents

<b>1</b>	<b>INTRODUCTION</b>	<b>4</b>
<b>2</b>	<b>FROM SINGLE MEDIUM TO DUAL-MEDIUM HYDROMECHANICAL COUPLING</b>	<b>5</b>
<b>2.1</b>	<b>REVIEW OF SINGLE MEDIUM HYDROMECHANICAL COUPLING SCHEME</b>	<b>5</b>
<b>2.2</b>	<b>DUAL-MEDIUM HYDROMECHANICAL COUPLING SCHEME</b>	<b>6</b>
2.2.1	<i>MECHANICAL DESCRIPTION OF THE DUAL POROUS MEDIUM</i>	6
2.2.2	<i>EXAMPLE OF PARAMETERS CALCULATION FOR A FRACTURED POROUS MEDIUM: FRACTURED SANDSTONE</i>	8
2.2.3	<i>FLUID FLOW DESCRIPTION OF THE DUAL POROUS MEDIUM AND COUPLING WITH MECHANICAL CALCULATION</i>	9
2.2.4	<i>ESTIMATION OF ROCK INTEGRITY</i>	12
<b>2.3</b>	<b>ILLUSTRATIONS - MODIFICATIONS OF THE HYDROMECHANICAL COUPLING</b>	<b>13</b>
2.3.1	TOY MODEL DESCRIPTION	13
2.3.2	BIOT THEORY – SIMPLE MEDIUM	15
2.3.3	DUAL MEDIUM RESULTS	16
<b>3</b>	<b>PRELIMINARY INVESTIGATION ON THERMAL EFFECTS ON GEOMECHANICAL BEHAVIOR IN CCS CONTEXT</b>	<b>20</b>
<b>3.1</b>	<b>MODEL ASSUMPTIONS AND LIMITATIONS</b>	<b>20</b>
<b>3.2</b>	<b>SYNTHETIC MODEL DESCRIPTION</b>	<b>20</b>
<b>3.3</b>	<b>RESULTS - SYNTHETIC MODEL</b>	<b>22</b>
<b>4</b>	<b>GROUND SURFACE RESPONSE ANALYSIS TO CO<sub>2</sub> LEAKAGE THROUGH A FRACTURED ZONE ABOVE THE INJECTION INTERVAL</b>	<b>25</b>
<b>4.1</b>	<b>SYNTHETIC MODEL</b>	<b>25</b>
<b>4.2</b>	<b>COUPLED HYDRO-MECHANICAL SIMULATOR</b>	<b>27</b>
<b>4.3</b>	<b>THE REFERENCE SCENARIO</b>	<b>27</b>
4.3.1	MODEL PARAMETERS:	27
4.3.2	REFERENCE SCENARIO RESULTS	28
4.3.3	CONCLUSION ON THE REFERENCE CASE	35
<b>4.4</b>	<b>SENSITIVITY ANALYSIS</b>	<b>35</b>
4.4.1	SENSITIVITY TO FAULT LENGTH	35
4.4.2	SENSITIVITY TO THE VERTICAL POSITION OF THE INJECTION WELL	36
4.4.3	SENSITIVITY TO SUB-SEISMIC FAULT COMPRESSIBILITY	36
4.4.4	SENSITIVITY TO TIME OF FRACTURE OPENING	37
4.4.5	SENSITIVITY TO SUB-SEISMIC FAULT PERMEABILITY INCREASE AT FRACTURE REOPENING	38
4.4.6	SENSIBILITY TO OVERBURDEN STIFFNESS	39
4.4.7	CONCLUSION ABOUT THE SENSITIVITY ANALYSIS	40
<b>5</b>	<b>SUMMARY AND CONCLUDING REMARKS</b>	<b>41</b>
	<b>BIBLIOGRAPHY</b>	<b>42</b>
	<b>ANNEX A - TABLES</b>	<b>43</b>
<b>1.</b>	<b>FIGURES TABLE</b>	<b>43</b>
	<b>ANNEX B - SUPPLEMENTARY FIGURES</b>	<b>45</b>

### 1 Introduction

The In Salah context was the main motivation to produce the work described in this report. Carbon dioxide has been injected in the Krechba field in Algeria between August 2004 and June 2011. Surface storage site has been monitored through InSAR technology during and after injection. An unexpected behavior has been encountered while injecting CO<sub>2</sub> with a CO<sub>2</sub> migration through a legacy well (KB-5) and a specific surface displacement footprint at one injection well (KB-502) described as a double-lobe deformation. This could be explained by a damaged zone that would allow a vertical migration of fluid through the caprock. According to White et al., 2013, this damaged zone could be a hydro-fractured zone triggered by the injection or a preexisting fractures zone (permeable or reactivated by the injection). In addition, In Salah storage formation has a low-permeable matrix but fractured medium. Based on previous studies (Deflandre et al., 2011), the modelling of a dual porous medium is required to be able to reproduce the storage behavior. For all these reasons, the In Salah site is a good candidate to study the effects of CO<sub>2</sub> injection on surface displacement and the potential of InSAR surface monitoring.

The purpose of this report is to describe the implementation of tools to reproduce the behavior observed on the In Salah site and a conceptual analysis of the physical phenomena that may have occurred on the storage site. The first development corresponds to the addition of functionality on the existing coupling tool to consider the "dual-medium" description of the injection site and its validation on a toy case. In a second step, a preliminary evaluation of the thermal effects induced by the injection of cold CO<sub>2</sub> in a warmer storage area has been performed. Finally, a conceptual approach has been implemented to reproduce a CO<sub>2</sub> leakage and the atypical surface behavior via a synthetic model with the opening of a fracture zone above the injection interval (without considering a dual-medium).

#### Nomenclature

$K$	<i>Bulk Modulus [Pa]</i>
$\mu$	<i>Shear Modulus [Pa]</i>
$E$	<i>Young Modulus [Pa]</i>
$\nu$	<i>Poisson Coefficient [-]</i>
$\varepsilon$	<i>Deformation (volumic) [-]</i>
$\sigma$	<i>Stress [Pa]</i>
$P$	<i>Pressure [Pa]</i>
$T$	<i>Temperature [°K]</i>
$\varphi$	<i>Porosity [-]</i>
$k$	<i>Permeability [mD]</i>
$\alpha$	<i>Thermal dilation coefficient [1/°C]</i>
$\underline{\underline{C}}$	<i>Elastic Tensor (4<sup>th</sup> order)</i>
$b$	<i>Biot coefficient [-]</i>
$C_p$	<i>Pore Compressibility [Pa<sup>-1</sup>]</i>
$M$	<i>Biot modulus [Pa<sup>-1</sup>]</i>
$\rho$	<i>Fluid density [kg.m<sup>-3</sup>]</i>

## 2 From single medium to dual-medium hydromechanical coupling

### 2.1 Review of single medium hydromechanical coupling scheme

The bases hypotheses are the following:

- The model is based on the framework of infinitesimal elastic strains
- The porous material is isotropic and fully saturated by a single fluid
- The porous medium is considered as the geometric superposition of two continuous media: a skeleton particle and a fluid particle (Figure 1)

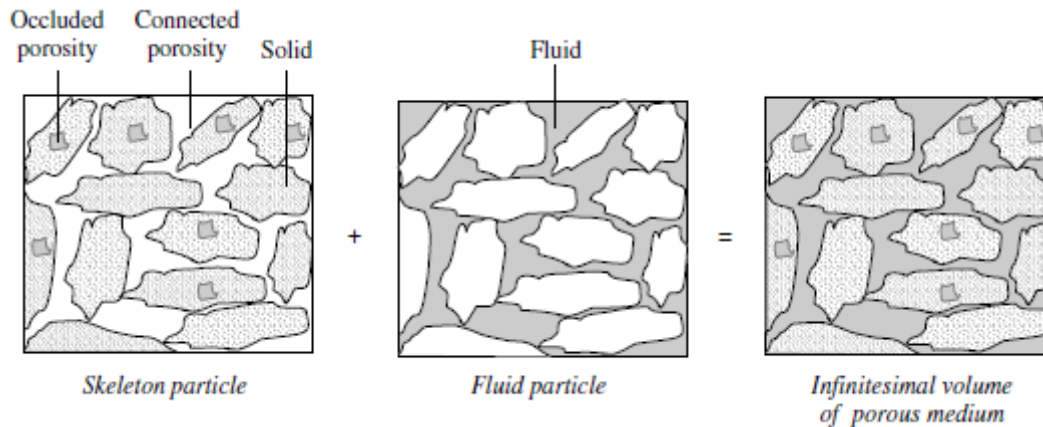


Figure 1 : Geometric description of the single-porosity porous medium (Coussy, 2004)

In this context, with the mechanical simulation, the variation of the stress field is calculated via equation 1<sub>a</sub> and variation in porosity as described in equation 2<sub>a</sub><sup>1</sup>

$$\underline{\underline{\Delta\sigma}} = \underline{\underline{C}} : \underline{\underline{\Delta\varepsilon}} - b \Delta P \underline{\underline{1}} - 3K^{hom} \alpha^s \Delta T^s \underline{\underline{1}} \quad (1a)$$

$$\Delta\varphi = b \text{tr} \underline{\underline{\Delta\varepsilon}} + \frac{\Delta P}{M} - 3\alpha^\varphi \Delta T^s \quad (2a)$$

The elastic tensor  $\underline{\underline{C}}$ , the Biot coefficient  $b$ , the Biot modulus  $M$  and the thermal expansion coefficient of the porous medium  $\alpha^\varphi$  are defined as follows:

$$\underline{\underline{C}} = 2\mu^{hom} \underline{\underline{1}} + \left( K^{hom} - \frac{2\mu^{hom}}{3} \right) \underline{\underline{1}} \otimes \underline{\underline{1}} \quad (3)$$

$$b = 1 - \frac{K^{hom}}{K^s} \quad (4)$$

$$\frac{1}{M} = \frac{b - \varphi}{K^s} \quad (5)$$

$$\alpha^\varphi = \alpha^s (b - \varphi) \quad (6)$$

With  $K^{hom}$  and  $\mu^{hom}$  the bulk and shear elastic moduli of the homogenized medium,  $K^s$  and  $\mu^s$  the bulk and shear elastic moduli of the solid matrix,  $\alpha^s$  the thermal expansion coefficient of the solid matrix and  $\varphi$  the porosity.

<sup>1</sup> Superscripts,  $s$  and  $hom$ , stand respectively for *skeleton* and *homogenized*

## Earth Sciences and Environmental Technologies Division

The homogenization between skeleton particle and fluid particle properties is obtained from Mori-Tanaka formulation:

$$K^{hom}(\varphi) = \frac{4K^S\mu^S(1-\varphi)}{3K^S\varphi+4\mu^S} \quad (4)$$

$$\mu^{hom}(\varphi) = \frac{\mu^S(1-\varphi)(9K^S+8\mu^S)}{K^S(9+6\varphi)+\mu^S(8+12\varphi)} \quad (5)$$

In our previous coupled simulations, we made the following assumptions for the coupling scheme:

- Incompressible matrix:  $K^S \rightarrow \infty \Rightarrow b = 1, M = \infty, \alpha^\varphi = 0$
- Isothermal evolution:  $\Delta T^S = 0$

Thus (1<sub>a</sub>) and (2<sub>a</sub>) become respectively  $\underline{\underline{\Delta\sigma}} = \underline{\underline{C}} : \underline{\underline{\Delta\varepsilon}} - \underline{\underline{\Delta p}} \underline{\underline{1}}$  (1<sub>b</sub>) and  $\Delta\varphi = \text{tr}\underline{\underline{\Delta\varepsilon}}$  (2<sub>b</sub>)

A simple example in paragraph 2.3.2 illustrates the impact of considering or not the solid matrix compressibility by comparing Biot vs. Terzaghi approaches for the stress variation calculation.

The coupling between hydro and mechanical calculation is performed for each time period of the fluid flow simulation, either iteratively (with retroaction between both simulators) or one-way (pressure results from fluid flow simulation is given to the mechanical simulator without any other interaction), see Deliverable D2.2 for details on the different coupling schemes.

The relationship between both simulators is defined through:

- a constant pore compressibility  $c_p$  defined in the fluid flow simulator as:

$$c_p = \frac{1}{\varphi} \left( \frac{b^2}{K^{hom}} + \frac{1}{M} \right) \xrightarrow{K^S \rightarrow \infty} c_p = \frac{1}{\varphi K^{hom}}$$

- $\Delta V_p$  linearly applied to the fluid flow simulator from the mechanical calculation throughout each simulation period (iterative coupling case)

## 2.2 Dual-medium hydromechanical coupling scheme

### 2.2.1 Mechanical description of the dual porous medium

The dual (porosity) medium is considered as the geometric superposition of three continuous media: a skeleton particle, a porous fluid particle and a fracture fluid particle (Figures 2 and 3).

## Earth Sciences and Environmental Technologies Division

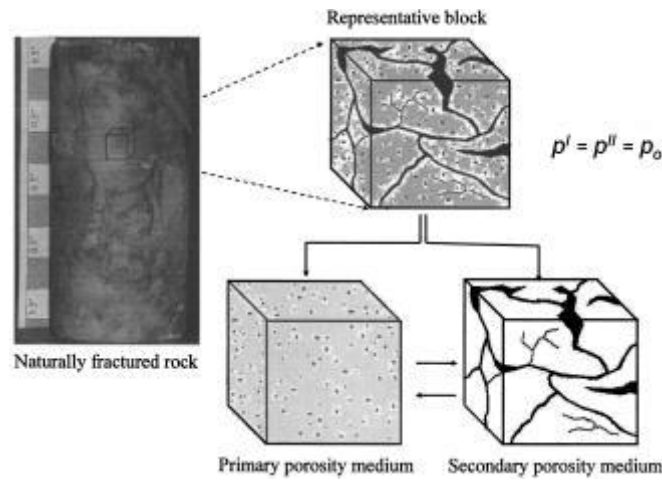


Figure 2 : Representation of the dual porosity medium for fractured rock (Abousleiman and Nguyen, 2005)

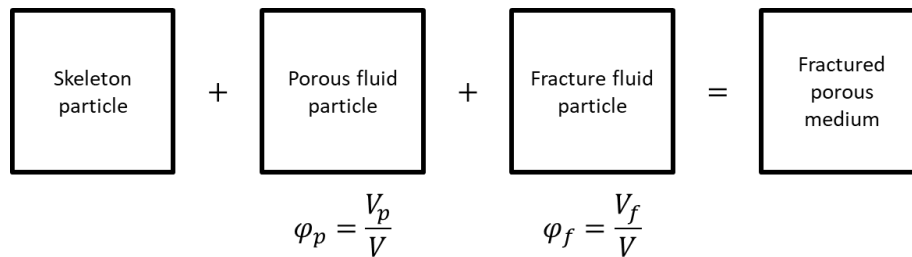


Figure 3 : Schematic description of the superposition of three continuous media (skeleton, porous and fracture)

With this description of the fractured medium, the variations of the stress field and porosity are calculated via equations 1<sub>c</sub>, 2<sub>c,p</sub> and 2<sub>c,f</sub>. Thus, the contribution from pressure variations become the weighted sum of pressure variations from both media and porosity variations are decomposed between fracture and porous/matrix media porosity variations.

$$\underline{\underline{\Delta\sigma}} = \underline{\underline{C}} : \underline{\underline{\Delta\varepsilon}} - b_p \Delta p_p \underline{\underline{1}} - b_f \Delta p_f \underline{\underline{1}} - 3K^{hom} \alpha^s \Delta T^s \underline{\underline{1}} \quad (1c)$$

$$\Delta\varphi_p = b_p \text{tr}\Delta\varepsilon + \frac{\Delta p_p}{M_{pp}} + \frac{\Delta p_f}{M_{pf}} - 3\alpha_p^\varphi \Delta T^s \quad (2_{c,p})$$

$$\Delta\varphi_f = b_f \text{tr}\Delta\varepsilon + \frac{\Delta p_p}{M_{fp}} + \frac{\Delta p_f}{M_{ff}} - 3\alpha_f^\varphi \Delta T^s \quad (2_{c,f})$$

The elastic tensor  $\underline{\underline{C}}$  is still given by equation 3, while Biot coefficients, Biot moduli, and thermal expansion coefficients are defined for both porous media:

$$b_p = \frac{K^{hom}}{K_p^{hom}} - \frac{K^{hom}}{K^s} \quad \text{and} \quad b_f = 1 - \frac{K^{hom}}{K_p^{hom}} \quad \text{with } b_p + b_f = b$$

$$\frac{1}{M_{pp}} = \frac{b_p - \varphi_p}{K^s} - (b_f - \varphi_f) \left( \frac{1}{K^s} - \frac{1}{K_p^{hom}} \right) \quad \text{and} \quad \frac{1}{M_{ff}} = \frac{b_f - \varphi_f}{K_p^{hom}}$$

$$\frac{1}{M_{fp}} = (b_f - \varphi_f) \left( \frac{1}{K^s} - \frac{1}{K_p^{hom}} \right) \quad \text{and} \quad \frac{1}{M_{pf}} = \frac{1}{M_{fp}}$$

$$\alpha_p^\varphi = \alpha^s (b_p - \varphi_p) \quad \text{and} \quad \alpha_f^\varphi = \alpha^s (b_f - \varphi_f)$$

With  $K^{hom}$ ,  $K_p^{hom}$ ,  $K^s$  respectively the bulk elastic moduli of the homogenized fractured medium, the homogenized unfractured medium and the solid matrix.

## Earth Sciences and Environmental Technologies Division

Homogenized properties for the fractured porous media are calculated assuming randomly oriented cracks with (Mori-Tanaka):

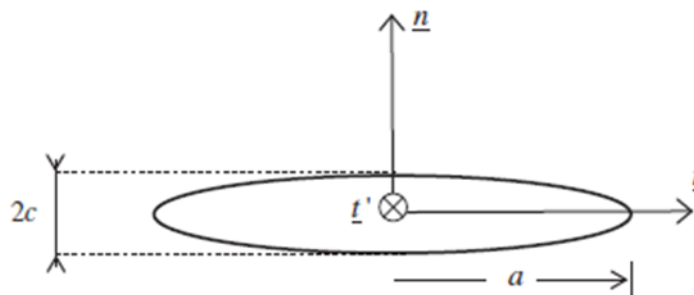
$$K^{hom}(\epsilon) = \frac{K_p^{hom}}{1 + \epsilon \frac{16(1-\nu_p^{2,hom})}{9(1-2\nu_p^{hom})}} \quad (4b)$$

$$\mu^{hom}(\epsilon) = \frac{\mu_p^{hom}}{1 + \epsilon \frac{32(1-\nu_p^{hom})(5-\nu_p^{hom})}{45(2-\nu_p^{hom})}} \quad (5b)$$

With  $\epsilon$  = crack density parameter

The crack density parameter ( $\epsilon$ ) is calculated based on the following fracture characteristics:

- Cracks are supposed to be oblate spheroids (Figure 4), defined by an aspect ratio  $X$ :
  - o  $X = \frac{c}{a}$  (aspect ratio)  $\rightarrow X \ll 1$
  - o With:
    - $c$  = half opening
    - $a$  = fracture radius
- With  $N$  = number of cracks per unit volume, the crack density parameter is calculated following
  - o  $\epsilon = Na^3$
- The volume fraction of cracks can then be calculated:
  - o  $\varphi_f = \frac{4}{3}\pi\epsilon X$



Crack as oblate spheroid

**Figure 4 : Schematic illustration of crack for considered fractured porous media**

Note: Results would be sensitive to the values of uncertain fracture characteristics such as  $c$  (half opening) and  $a$  (fracture radius) parameters.

If crack density parameter  $\epsilon$  is zero,  $K^{hom} = K_p^{hom}$ , the simple medium formulation is obtained by simplification of the dual medium equations.

### 2.2.2 Example of parameters calculation for a fractured porous medium: fractured sandstone

Assuming the following characteristics for the fractured porous medium:

$$\begin{aligned} N &= 8 & \epsilon &= 1 \\ a &= 0.5 \text{ m} & \Rightarrow & X = 0.002 \\ c &= 0.001 \text{ m} & & \varphi_f = 0.84\% \end{aligned}$$



## Earth Sciences and Environmental Technologies Division

Fractured sandstone	Non fractured sandstone
$\varphi_p = 25\%$	$\varphi_p = 25\%$
$s\varphi_f = 0.84\%$	$\varphi_f = 0\%$
$K^{hom} = 1.98 \text{ GPa}$	$K_p^{hom} = 10 \text{ GPa}$
$\mu^{hom} = 1.94 \text{ GPa}$	$\mu_p^{hom} = 4.62 \text{ GPa}$
$b_p = 0.1$ $b_f = 0.8$	$b_p = 0.5$
$M_{pp} = 31.12 \text{ GPa}$ $M_{ff} = 12.60 \text{ GPa}$ $M_{pf} = -25.20 \text{ GPa}$	$M_{pp} = 80 \text{ GPa}$
$\alpha_p^\varphi = -0.15 \times 10^{-5} \text{ }^\circ\text{C}^{-1}$ $\alpha_f^\varphi = 0.79 \times 10^{-5} \text{ }^\circ\text{C}^{-1}$	$\alpha_p^\varphi = 0.25 \times 10^{-5} \text{ }^\circ\text{C}^{-1}$


In case some considers an incompressible matrix  $K^S \rightarrow \infty$ , coefficients become:

$$b_p = \frac{K^{hom}}{K_p^{hom}} \quad b_f = 1 - \frac{K^{hom}}{K_p^{hom}} \quad b_p + b_f = b = 1$$

$$\frac{1}{M_{pp}} = \frac{b_f - \varphi_f}{K_p^{hom}} \quad \frac{1}{M_{ff}} = \frac{1}{M_{pp}} \quad \frac{1}{M_{pf}} = \frac{1}{M_{fp}} = -\frac{b_f - \varphi_f}{K_p^{hom}} = -\frac{1}{M_{pp}}$$

$$\alpha_p^\varphi = 0 \quad \alpha_f^\varphi = 0$$

Now, if we compare coefficients values between compressible and incompressible matrix cases for our previous example of fractured porous media, it comes:

$b_p = 0.1$	$b_f = 0.8$	$K^S \rightarrow \infty$	$b_p = 0.2$	$b_f = 0.8$
$M_{pp} = 31.12 \text{ GPa}$	$M_{ff} = 12.60 \text{ GPa}$		$M_{pp} = 12.60 \text{ GPa}$	
$M_{pf} = -25.20 \text{ GPa}$			$M_{pf} = -12.60 \text{ GPa}$	

### 2.2.3 Fluid flow description of the dual porous medium and coupling with mechanical calculation

The dual-medium concept used in the fluid flow simulator is based on an ideal description of fractured reservoir after Warren and Root, 1963 (Figure 5). Two superimposed mesh (fracture and porous/matrix media) are defined with different properties (porosity  $\varphi$  and permeability  $k$ ) in each medium:

- A matrix mesh with  $\varphi_p, k_p$
- A fractured mesh with  $\varphi_f, k_f$
- Fractured network is connected
- An exchange term is defined between superposed cells fracture <-> matrix (function of blocks sizes) (Figure 5)
- Flow is allowed in both media (Figure 6)

## Earth Sciences and Environmental Technologies Division

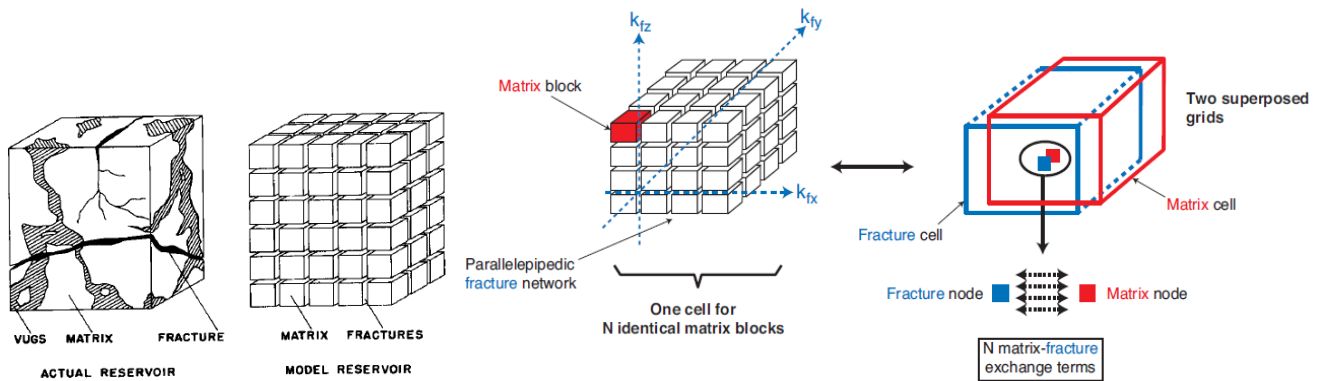


Figure 5 : Left, schematic representation of the dual-medium concept after Warrant and Root (1963). Illustration of the superposed mesh for representing the dual-medium with the flow simulator, PumaFlow (IFP Energies Nouvelles, 2018).

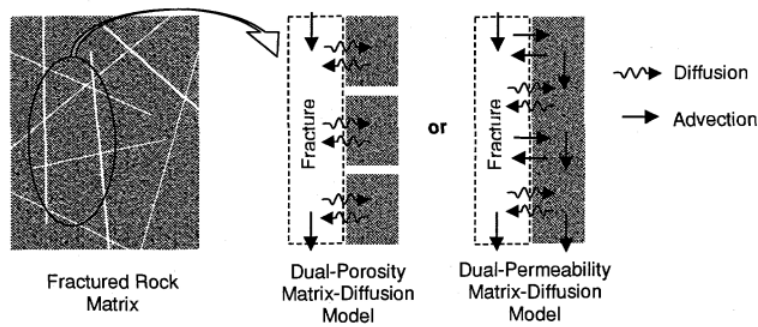


Figure 6 : From Ho (2000), illustration of two alternative conceptual models for matrix diffusion in fractured rocks: either no flow between matrix blocks (*i.e.*, only matrix-fracture flow) or flow is allowed in both media.

For consistency between both calculations (hydro and mechanical), pore compressibility should be defined following:

$$c_p = \frac{1}{\varphi_p} \left( \frac{b_p^2}{K^{hom}} + \frac{1}{M_{pp}} \right) \qquad c_f = \frac{1}{\varphi_f} \left( \frac{b_f^2}{K^{hom}} + \frac{1}{M_{ff}} \right)$$

In the iterative coupling case,  $\Delta V_p$  and  $\Delta V_f$  are applied in each mesh.

Notice that homogenized properties such as compressibility and mechanical rock properties will strongly depend on poorly known properties such as shape factor, fracture porosity as shown in Figures 7 and 8. The inversion from homogenized value such as Young modulus  $E_h$  and poisson ratio  $\nu_h$  to  $K_s$ ,  $G_s$  is not straightforward without strong hypotheses on fracture medium properties for example (Figure 7). Results are obtained from an iterative coupling between flow simulator PumaFlow and mechanical simulator Code\_Aster based on the dual medium scheme described in section 2.2.1.

## Earth Sciences and Environmental Technologies Division

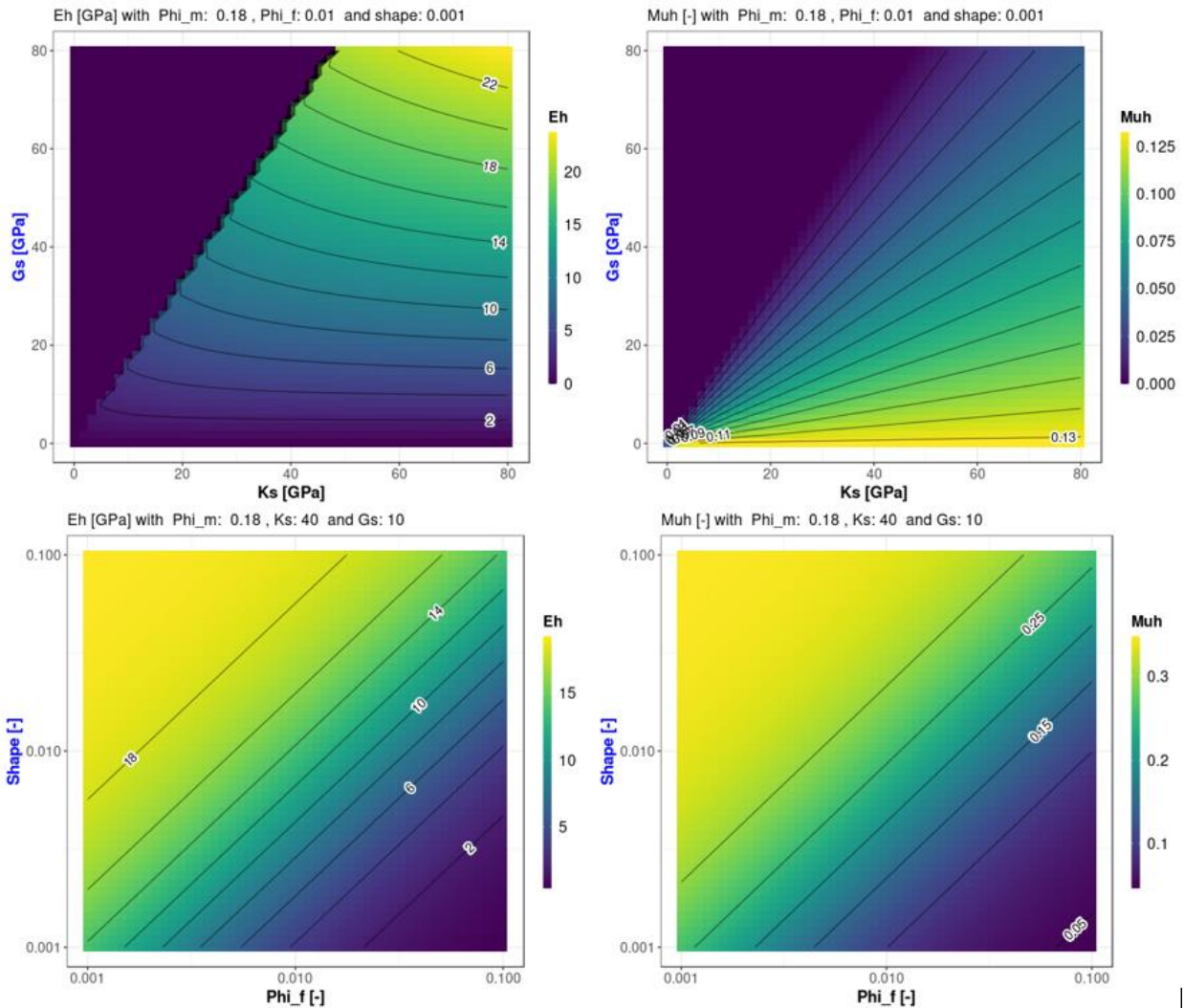


**Figure 7 : Homogenized Young Modulus and Poisson coefficient for dual-medium, function of skeleton shear and bulk moduli (top) and function of fracture porosity and shape factor (bottom). Inadmissible values, such as Poisson coefficient is negative, were nullified.**



## Earth Sciences and Environmental Technologies Division

$$\Delta \underline{\underline{\sigma}}' = \Delta \underline{\underline{\sigma}} + \Delta p \underline{\underline{1}} = \underline{\underline{C}} : \Delta \underline{\underline{\varepsilon}} + (1 - b) \Delta p \underline{\underline{1}} - 3K^{hom} \alpha^s \Delta T \underline{\underline{s}}_1$$

Equation 2 : Terzaghi effective stress, for failure criterion calculation

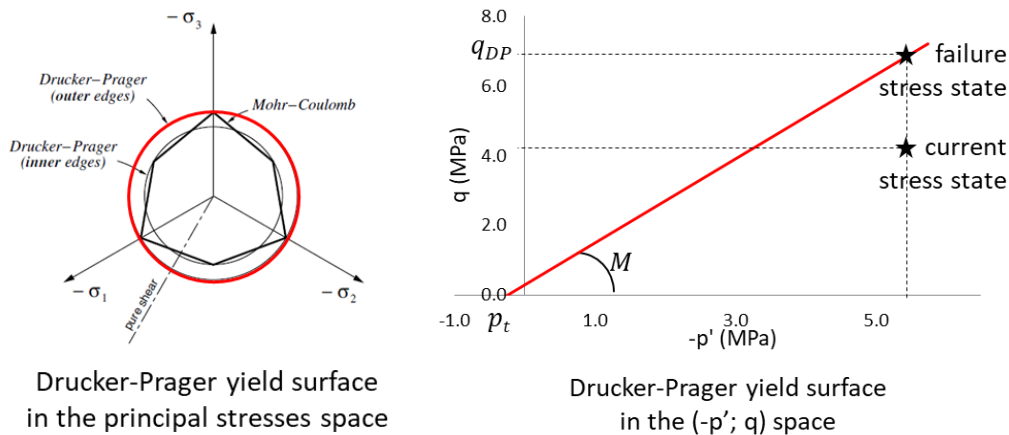


Figure 9 : Drucker-Prager yield surfaces in the deviatoric plane and projection in  $(-p', q)$  space with  $p'$  = mean effective stress and  $q$  = deviatoric stress.

## 2.3 Illustrations - modifications of the hydromechanical coupling

### 2.3.1 Toy model description

Main model characteristics (Figure 10):

- 10 x 10 x 2.15 km (symmetrical planes at  $x=0$  and  $y=0$ )
- 20 x 20 x 14 cells (5600 cells)
- From top to bottom:
  - 1.4 km of overburden (« flow- inactive »)
  - 380 m of seal rocks (10 m at the reservoir interface are dual-medium for the dual-medium case)
  - 40 m of reservoir
  - 250 m of underburden (200 m are « flow-inactive »)
- 2-phases flow
- Total injection period: 1 year
- Maximum increase in BHP: 100 bars
- Maximum CO<sub>2</sub> injection rate:  $1.5 \cdot 10^6 \text{ sm}^3/\text{d}$
- Isothermal calculations
- Numerical flow resolution uses 9-pts scheme
- Only the one-way coupling scheme has been used for this study
- Initial conditions:
  - $\sigma'_h / \sigma'_v = \sigma'_H / \sigma'_V = 0.8$
  - $P = 20 \text{ MPa @ } 2000\text{m}$
- Boundary conditions:
  - Oedometric conditions
  - Bottom, top, and lateral surfaces are impermeable
  - A large porous volume is defined for lateral boundary cells to mimic open lateral boundary conditions
- Post-process failure evaluation: Friction angle =  $25^\circ$  and  $c = 1.E+06 \text{ Pa}$

## Earth Sciences and Environmental Technologies Division

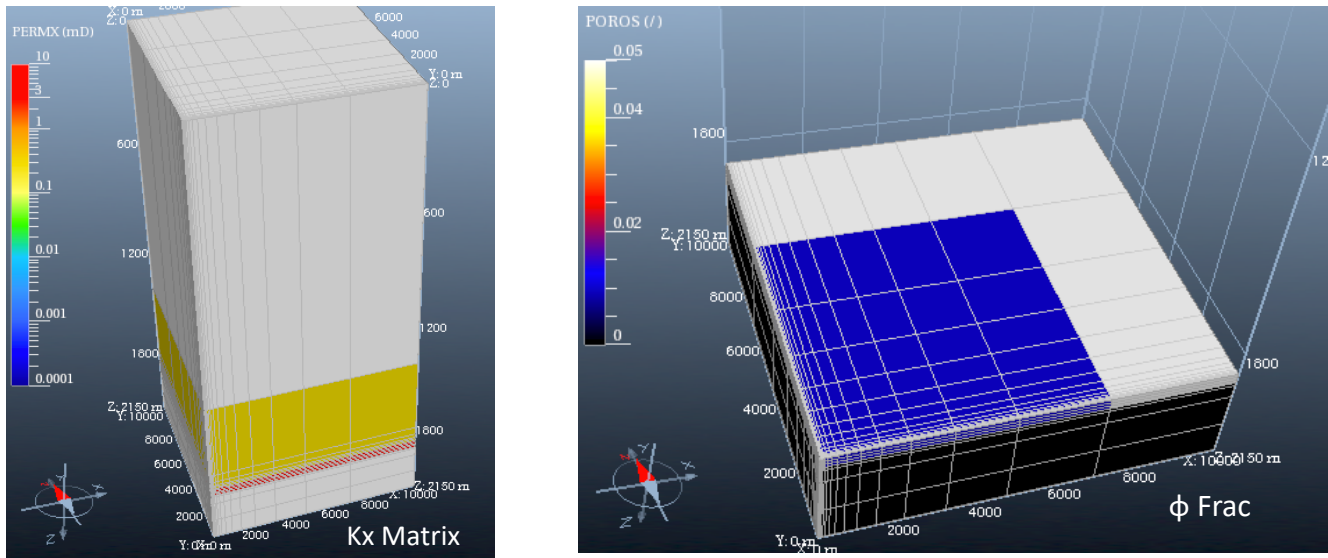


Figure 10 : Illustration of the toy model with the injection point at the left corner (equivalent to a quarter five-spot, with only one injection well).

Table 1 : Rock properties for the single medium case

Layer from top to bottom	Thickness	“Medium type”, if relevant	$\phi_p$ [-]	$k_{xp}$ [mD]	$k_{zp}$ [mD]	$E_s$ [GPa]	$\nu_s$ [-]
1	1400	Inactive	0	0	0	13.54	0.26
2	380	Simple Medium	0.05	0.3	0.03	13.54	0.26
3	40	Simple Medium	0.05	0.3	0.03	13.54	0.26
4	20	Simple Medium	0.05	0.3	0.03	13.54	0.26
5	10	Simple Medium	0.05	0.3	0.03	13.54	0.26
6	10	Dual Medium	0.05	0.3	0.03	13.54	0.26
7	10	Dual Medium	0.18	30	3	13.54	0.26
8	10	Dual Medium	0.18	30	3	13.54	0.26
9	10	Dual Medium	0.18	30	3	13.54	0.26
10	10	Dual Medium	0.18	30	3	13.54	0.26
11	10	Simple Medium	0.01	1.00E-04	1.00E-05	13.54	0.26
12	40	Simple Medium	0.01	1.00E-04	1.00E-05	13.54	0.26
13	100	Inactive	0	0	0	13.54	0.26
14	100	Inactive	0	0	0	13.54	0.26

Specific characteristics of the dual-medium cases:

- Only some model layers are considered as “dual medium”, see table 1
- Only capillary and gravity effects are considered for Fracture-Matrix Exchange (valid if the viscous effects are negligible comp. w. capillary & gravity effects, *i.e.* when fracture conductivity is high enough)
- Blocks sizes: 10x10x1m
- Several rock properties scenarios for fractured media are considered:

## Earth Sciences and Environmental Technologies Division

- One pseudo simple medium to control the coupling results with low fracture porosity and permeability (0.001% and 1.E-10 mD, resp.)
- Several scenarios with different fracture permeability (see table 2)

**Table 2 : Parameters values for the different simple-medium and dual-medium cases<sup>2</sup>**

	Simple Medium	Dual Medium 1	Dual Medium 2	Dual Medium 3a	Dual Medium 3b
$\varphi_p$ [-]	18%	18%	18%	18%	18%
$\varphi_f$ [-]	0%	0.001%	1%	1%	1%
$k_p$ [md]	30.0	30.0	30.0	30.0	30.0
$k_f$ [md]	0.0	1.00E-10	1.00E-10	3.00E+01	3.00E+02
$E^{hom}$ [GPa]	9.4	9.36	1.81	1.81	1.81
$\nu^{hom}$ [-]	0.25	0.25	0.07	0.07	0.07
$b_p$ [-]	0.34	0.33	0.04	0.04	0.04
$b_f$ [-]	0	0.01	0.88	0.88	0.88

### 2.3.2 Biot theory – Simple medium

The simple medium case is used to confront the Biot vs. Terzaghi theories of elasticity, *i.e.*, what are the consequences of neglecting the solid matrix compressibility when calculating the surface uplift and risk of failure for CCS project.

The Biot approach leads to less deformation and consequently to a reduce uplift (Figure 11). For the studied case, the Terzaghi approach tends to underestimate the failure risk (Figure 12). We also observe a significant difference in dynamic behaviors between both approaches.

To summarize, adopting the Biot formulation provided less deformation (uplift) and more rock failure risk. This approach is more conservative and would be recommended in a risk analysis point of view.

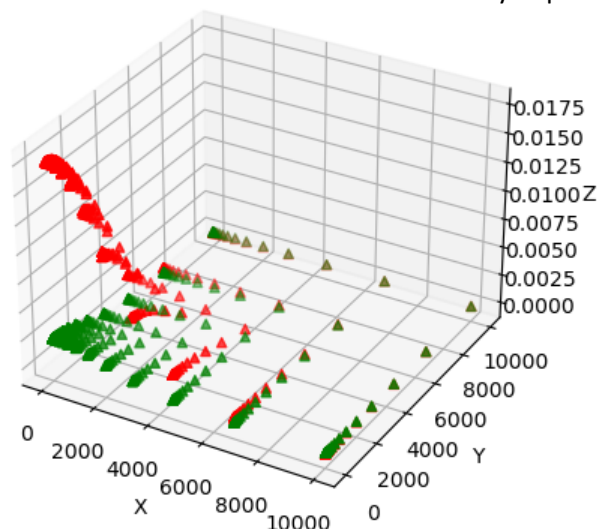


**Figure 11 : Cumulative surface displacement when considering Terzaghi formulation (red) or Biot formulation (green) for the simple medium case after one year of injection.**

- <sup>2</sup> Fractured media properties have been calculated using fracture aspect ratio  $X = 0.001$ 
  - This value highly impacts the elastic coefficients even for low fracture porosities ~1%
  - It could have been interesting to use  $X = 0.01$  depending on the studied case

## Earth Sciences and Environmental Technologies Division

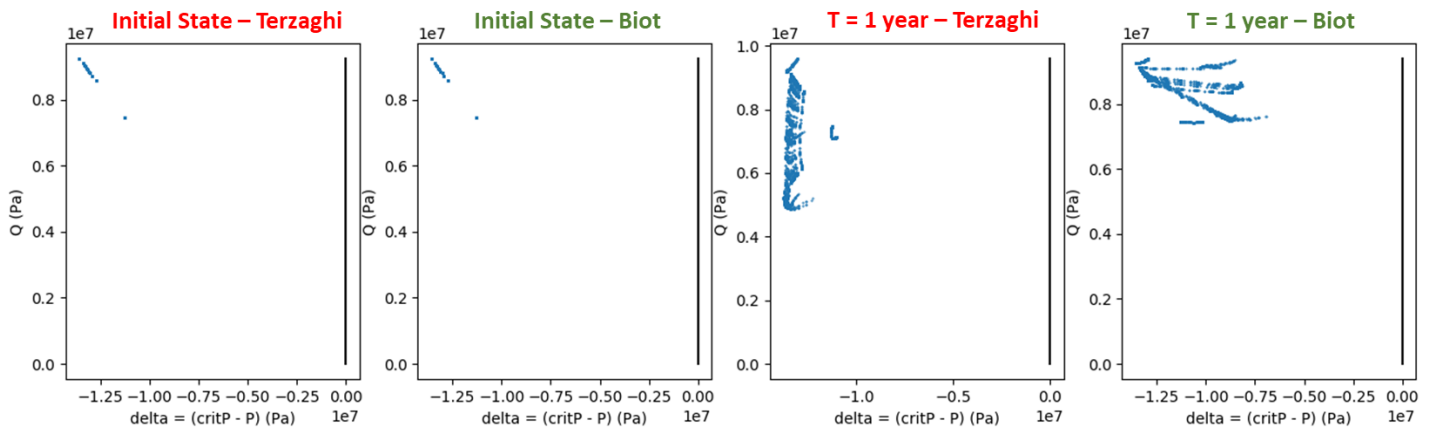


**Figure 12 : Evolution of the stress state from the initial state (left) to after one year of injection (right) in (delta p, q) representation, for the Biot and Terzaghi approaches. Each point represents an element. If one of them cross the black line on the right (delta = 0), the failure criterion is reached.**

### 2.3.3 Dual medium results

Several cases are considered:

1. Validation of the coupling: Simple medium vs. equivalent dual medium (low porosity and permeability fractures – Dual Medium 1 in table 2)

No significant differences are obtained from both cases (Figures 13 and 14) as expected from a valid coupling for both schemes with these cases definition.

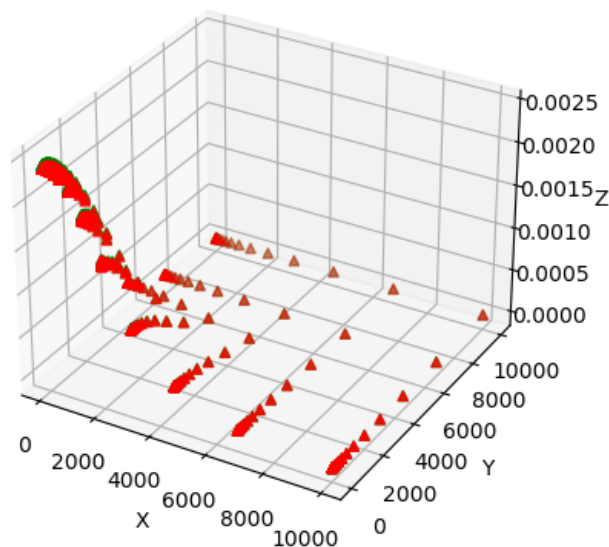


**Figure 13 : Cumulative surface displacement for the simple medium (red) or dual medium 1 (green) after one year of injection.**



## Earth Sciences and Environmental Technologies Division

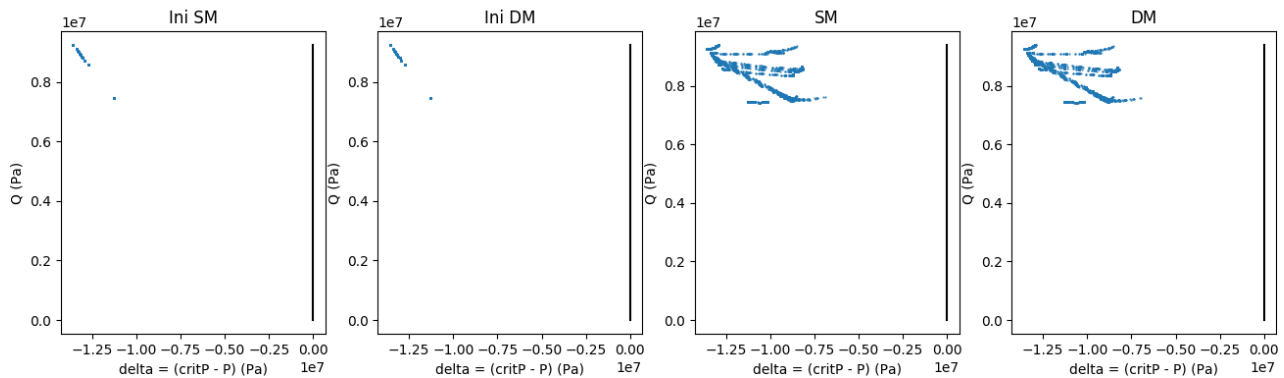


**Figure 14 : Evolution of the stress state from the initial state (left) to after one year of injection (right) in ( $\Delta p$ ,  $q$ ) representation, for the simple medium (SM) and dual medium (DM) cases. Each point represents an element. If one of them crosses the black line on the right ( $\Delta = 0$ ), the failure criterion is reached.**

2. Dual medium with low fracture permeability: fracture effects on geomechanics only (fracture porosity – Dual Medium 2 in table 2)

No significant changes are observed in flow behavior between dual medium 1 and dual medium 2 cases (only change in fracture porosity, fracture permeability is still very low:  $1e-10$  mD). Thus, the observed differences in surface displacement (Figure 15) are mainly due to the change in rock mechanical properties while changing fracture porosity: in particular, homogenized Young modulus reduces over almost one order of magnitude, this means a softer rock resulting in higher deformation and consequently a higher surface displacement, despite a weaker Biot coefficient in matrix. The same remarks apply for the stress evolution (Figure 16), while the flow constraint remain the same (i.e., increase in pressure, injected volume), rock properties reduce drastically with the increase in fracture porosity (shear and bulk moduli, matrix biot coefficient) leading to more scattered results, further away from the failure criterion.

These results underline the high sensitivity of mechanical behavior to the dual medium rock properties definition.

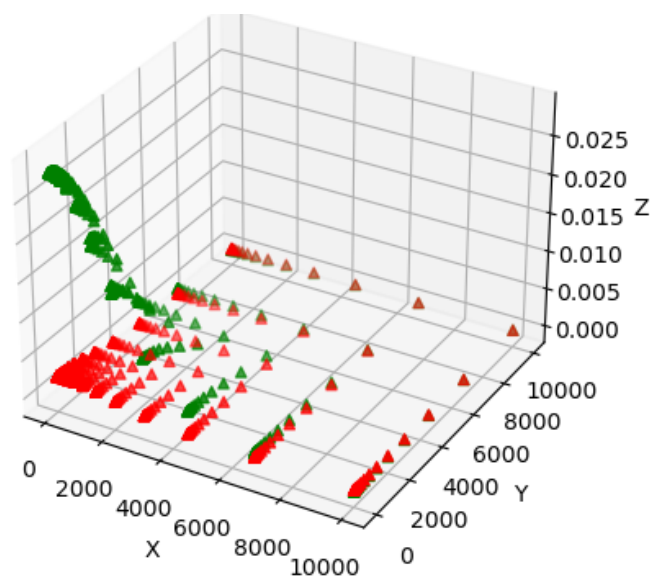


**Figure 15 : Cumulative surface displacement for the dual medium 1 ( $\phi_f=1e-5$ , red) or dual medium 2 ( $\phi_f=1e-2$ , green) after one year of injection.**

## Earth Sciences and Environmental Technologies Division

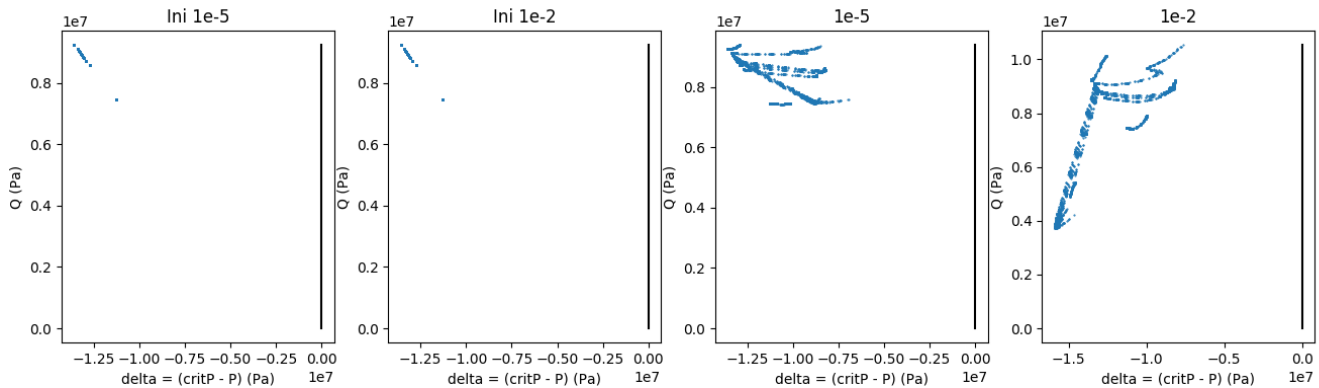


**Figure 16 : Evolution of the stress state (from the initial state (left) to after one year of injection (right) in ( $\delta p$ ,  $q$ ) representation, for the dual medium 1 ( $\varphi_f=1e-5$ ) and 2 ( $\varphi_f=1e-2$ ) cases. Each point represents an element. If one of them cross the black line on the right ( $\delta = 0$ ), the failure criterion is reached.**

### 3. Dual medium with high fracture permeability: combined fracture effects (Dual Medium 3a and 3b in table 2)

For both cases, Dual medium 3a and 3b, the rock mechanical properties remain the same as for the Dual medium 2 case. The differences, this time, are not due to rock mechanical properties but rather due to flow properties and consequent flow behavior. From 2 to 3a cases, because of the increase in fracture permeability, a higher amount of  $CO_2$  is injected for a lower increase in pressure (Figure 20). This leads to a lower increase in surface displacement close to the well but slightly higher further away from the well (Figure 17). Moreover, because of the lower overpressure, the risk of failure decreases (Figure 18).

From case 3a to 3b, the fracture permeability is again increased but this time does not result in an increase in the amount of injected  $CO_2$  because of the maximum injection rate limitation. The quantity is the same, but the pressure build-up is lower for the 3b case with the highest permeability (Figure 20). Therefore, the uplift for the case with the highest permeability is even lower than previously (Figure 17) and, again, the risk of failure decreases because of the lower overpressurization (Figure 19).

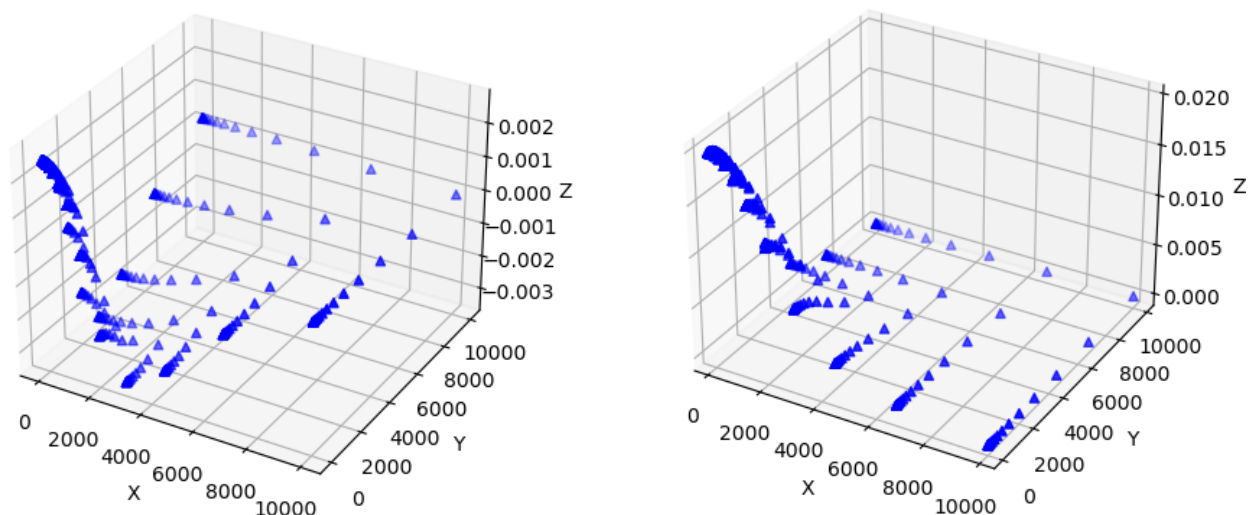


**Figure 17 : Differences in surface displacement between (Left) the dual medium 2 and dual medium 3a ( $k_f=30$  md,) and (Right) the dual medium 3a and dual medium 3b ( $k_f=300$  md) after one year of injection.**

## Earth Sciences and Environmental Technologies Division

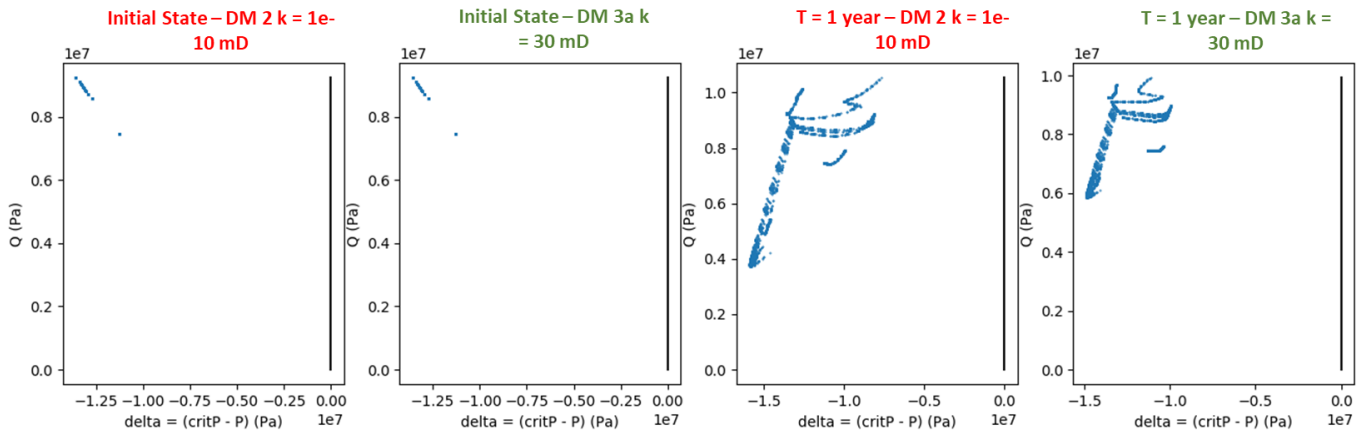


**Figure 18 :** Evolution of the stress state from the initial state (left) to after one year of injection (right) in  $(\Delta p, q)$  representation, for the dual medium 2 ( $k_f=1e-10$  mD) and 3a ( $k_f=30$  mD) cases. Each point represents an element. If one of them cross the black line on the right ( $\Delta p = 0$ ), the failure criterion is reached.

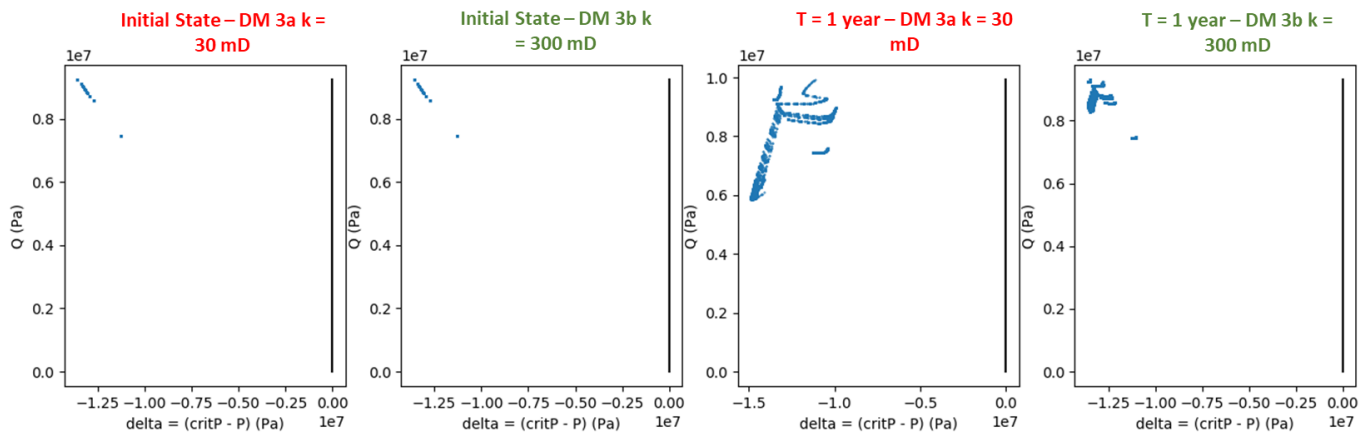


**Figure 19 :** Evolution of the stress state from the initial state (left) to after one year of injection (right) in  $(\Delta p, q)$  representation, for the dual medium 3a ( $k_f=30$  mD) and 3b ( $k_f=300$  mD) cases. Each point represents an element. If one of them cross the black line on the right ( $\Delta p = 0$ ), the failure criterion is reached.

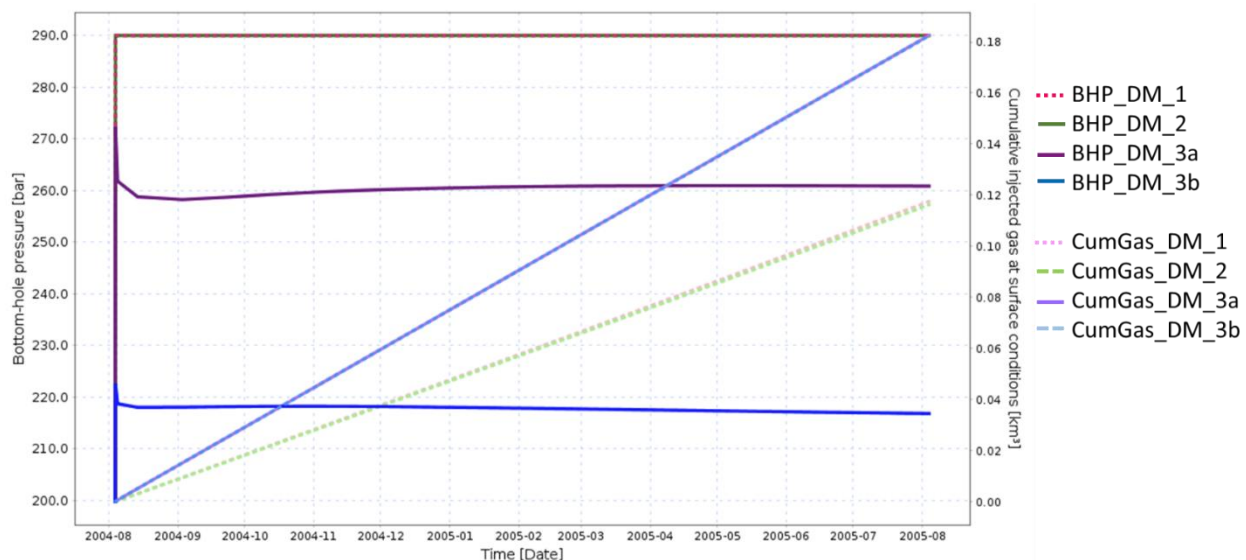


**Figure 20 :** BHP and cumulative gas injection at surface conditions function of time for the different studied Dual-medium cases.

### 3 Preliminary investigation on thermal effects on geomechanical behavior in CCS context

The objective is to investigate the thermal effects when performing geomechanical analysis of CO<sub>2</sub> underground storage. More specifically, we study the effect on surface displacement and subsurface storage integrity while injecting a cooler fluid than in-place temperature.

A synthetic model is used to simulate the thermo-hydromechanical evolution of a reservoir and the above seal rocks during one year of CO<sub>2</sub> injection at constant rate. Some parameters may seem exaggerated regarding real case applications (geometry, injection rate, overpressure generation, temperature decrease): the set of parameters has been chosen to illustrate the physics provided by the new formulation (as described in the first section of this report). Simulations were performed by an internal tool developed by Andre Bruch.

#### 3.1 Model assumptions and limitations

- Infinitesimal elastic strains
- Isotropic material
- **Simple / Single porosity medium**
- Fully saturated by a **single compressible fluid (water)**
  - o Pressure induced by the CO<sub>2</sub> injection is modelled by means of a water source term
- Fluid and skeleton are in thermal equilibrium
  - o Cooling induced by the CO<sub>2</sub> injection is modelled by means of a heat sink term
- Plastic yield surface is used to evaluate seal rock integrity
  - o Matrix plastic incompressibility: failure is controlled by Terzaghi effective stress (see paragraph 2.2.4)
- Recall of the constitutive equations for these thermo-hydro-mechanical calculations:

● **Constitutive equations of the skeleton:**

$$\underline{\underline{\Delta \underline{\underline{\sigma}}}} = \underline{\underline{C}} : \underline{\underline{\Delta \underline{\underline{\varepsilon}}}} - b \Delta p \underline{\underline{1}} - 3K^{hom} \alpha^s \Delta T^s \underline{\underline{1}}$$

$$\Delta \varphi = b \text{tr} \underline{\underline{\Delta \underline{\underline{\varepsilon}}}} + \frac{\Delta p}{M} - 3\alpha^\varphi \Delta T^s$$

● **Classical poroelasticity coefficients:**

$$\underline{\underline{C}} = 2\mu \underline{\underline{1}} + \left( K - \frac{2\mu}{3} \right) \underline{\underline{1}} \otimes \underline{\underline{1}} \quad b = 1 - \frac{K^{hom}}{K^s}$$

$$\frac{1}{M} = \frac{b - \varphi}{K^s} \quad \alpha^\varphi = \alpha^s (b - \varphi)$$

● **Constitutive equation of the fluid:**

$$\rho^f = \rho_0^f \exp\left(\frac{\Delta p}{K^f} - 3\alpha^f \Delta T^f\right)$$

● **Conversion formulae:**

$$K = \frac{E}{3(1 - 2\nu)} \quad \mu = \frac{E}{2(1 + \nu)}$$

#### 3.2 Synthetic model description

Model is defined as (Figure 21):

- 10 x 10 x 2.5 km (symmetry planes at x=0 and y=0)
- From top to bottom:
  - o 2km of overburden
  - o 100m of seal rocks
  - o 200m of reservoir
  - o 200m of underburden
- Total time: 1 year
- Time-step: 1 week
- Fluid mass source: 2.5 Mton/year
- Heat sink: -3 W/m<sup>3</sup>

## Earth Sciences and Environmental Technologies Division

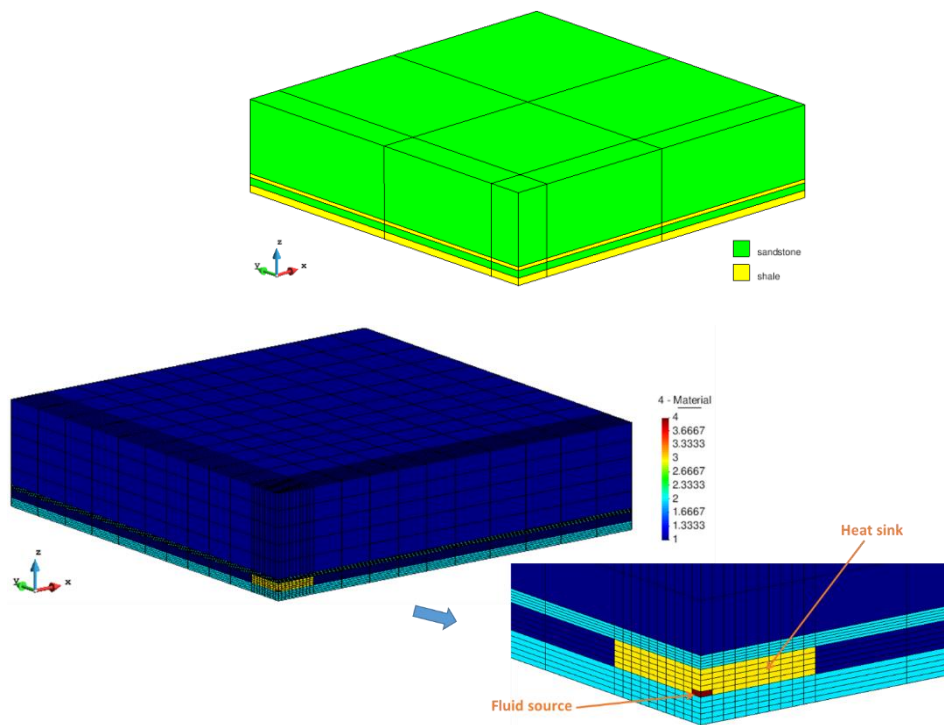


Figure 21 : Illustration of the synthetic model with the injection point at the left corner (equivalent to a quarter five-spot, with only one injection well) and with two facies: sandstone for the injection zone and the shallower aquifer/overburden (up-to the surface) and shale for the caprock and underburden.

- Post-process failure evaluation: Friction angle = 30° and  $c = 0$
- Initial conditions (Figure 22):
  - Geostatic equilibrium
    - $\sigma'_h / \sigma'_v = \sigma'_H / \sigma'_v = 0.66$
  - Hydrostatic pressure
    - $p = \rho^f g z$
  - Geothermal equilibrium
    - $T^{top} = 20^\circ\text{C}$
    - $\partial T / \partial z = 40^\circ\text{C/km}$
- Boundary conditions:
  - Oedometric conditions
  - $p^{top} = 0$
  - Bottom and lateral surfaces are impermeable
  - $T^{top} = 20^\circ\text{C}$ ;  $q^{bottom} = 80 \text{ mW/m}^2$
  - Lateral surfaces are insulated

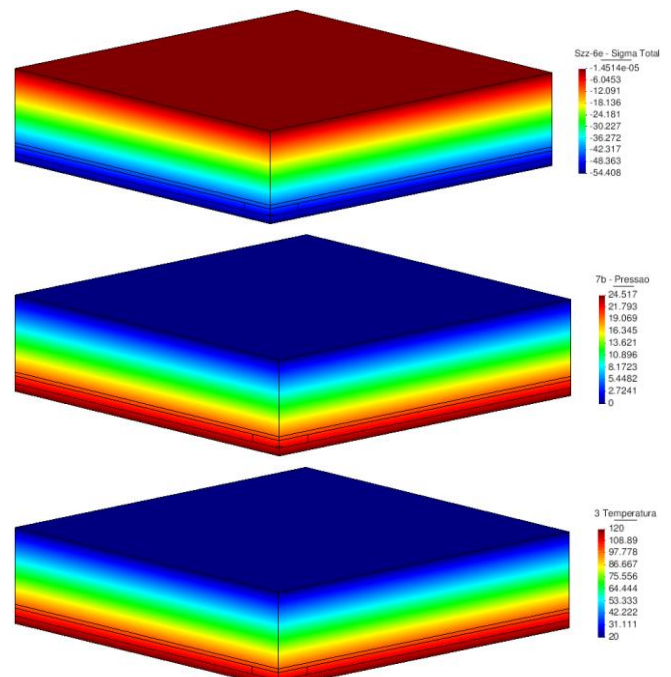


Figure 22 : Initial conditions. From top to bottom: Total stress [MPa], Pressure [MPa] and Temperature [°C].

Porous material properties are summarized in table 3. Fluid properties are summarized in table 4.

## Earth Sciences and Environmental Technologies Division

**Table 3 : Porous material properties**

Parameter	Symbol	Sandstone	Shale
Porosity	$\phi$	0.25	0.15
Density (kg/m <sup>3</sup> )	$\rho$	2200	2360
Young modulus (MPa)	E	12000	25000
Poisson's ratio	$\nu$	0.3	0.25
Biot coefficient	b	0.50	0.29
Biot modulus (MPa)	M	80000	168120
Thermal dilation coef. of solid phase (1/°C)	$\alpha^s$	1.00E-05	1.00E-05
Thermal dilation coef. of pores (1/°C)	$\alpha^p$	0.25E-05	0.14E-05
Permeability (m <sup>2</sup> )	$k^f$	1E-13	5E-18
Specific heat (J/kg°C)	c	1500	1500
Thermal conductivity coefficient (W/m°C)	$k^t$	2	2
Volume heat generation (W/m <sup>3</sup> )	r	0	0

**Table 4 : Fluid properties**

Parameter	Symbol	Value
Density of fluid (kg/m <sup>3</sup> )	$\rho_0^f$	1000
Bulk modulus (MPa)	$K^f$	2200
Thermal dilation coefficient(1/°C)	$\alpha^f$	7.00E-05
Specific heat (J/kg°C)	$c^f$	4200
Thermal conductivity (W/m°C)	$k^{t,f}$	0.6

### 3.3 Results - synthetic model

The major cooling effect occurs in the injection zone (figure 23) but is also observed in the first seal elements (figure 24) with a decrease of temperature about 30°C in 1 year.

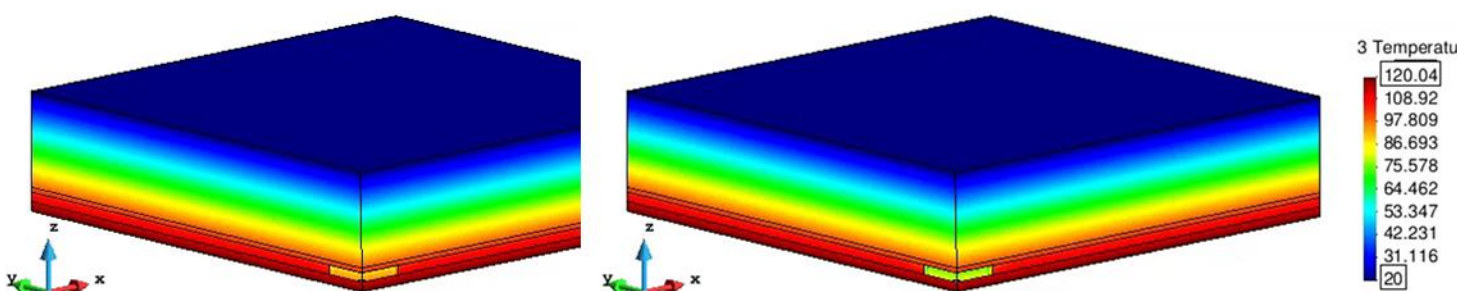


**Figure 23 : Temperature evolution [°C] at 0.5 year (left) and one year (right).**

## Earth Sciences and Environmental Technologies Division

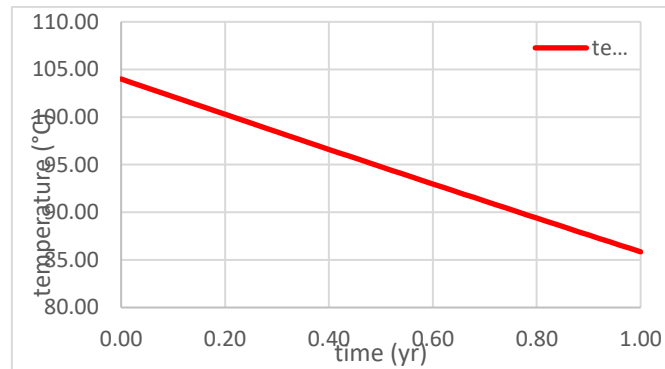


**Figure 24 : First seal rock element temperature evolution with time.**

This temperature variation induces an increase in the horizontal effective stress and a slight change in overpressure while no significant changes affect the vertical effective stress when comparing isothermal and thermo-hydrromechanical (THM) coupling results (Figure 25). In the considered initial stress state (extensional), this thermal effect on the horizontal effective stress will increase the deviatoric stress  $q$  and may cause to reach the failure criterion as in Figure 25, thus increase the risk of rock failure. In other words, in this context, neglecting the thermal effect when injecting cold  $\text{CO}_2$  may underestimate the risk for caprock integrity.

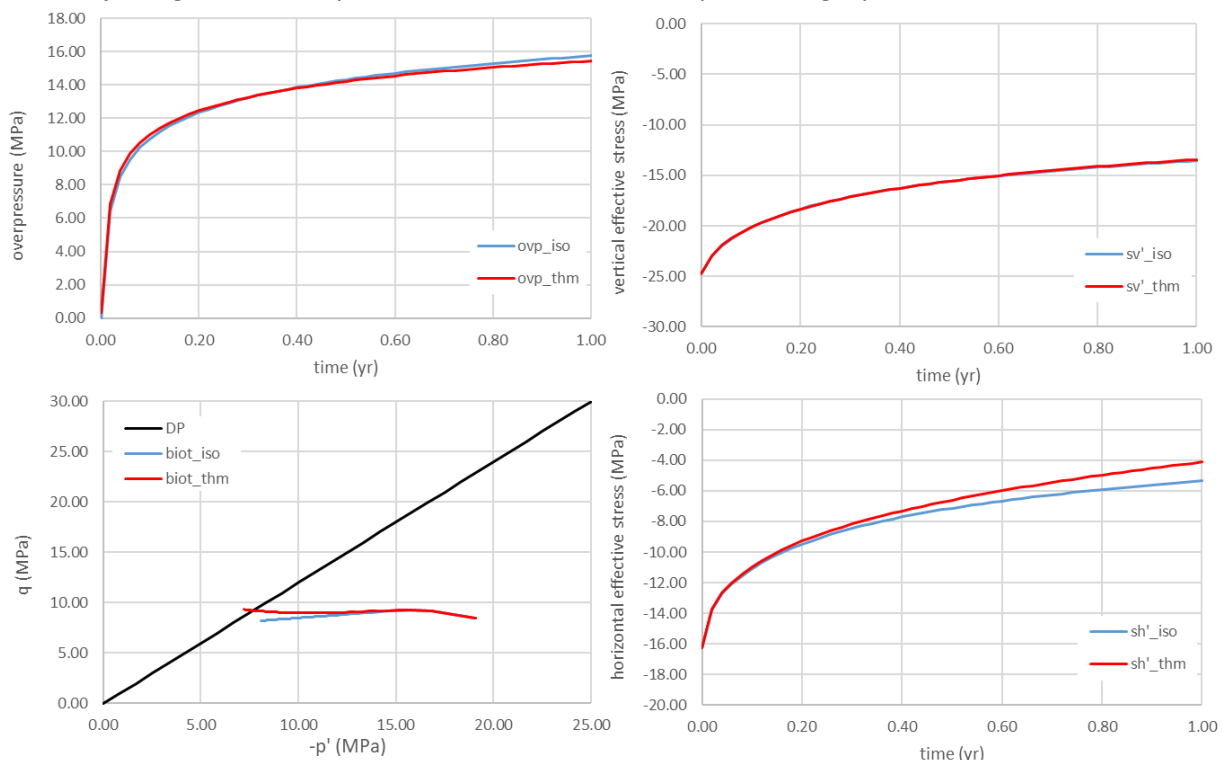


**Figure 25 : Comparison between isothermal and THM simulation results for the first seal rock element overpressure (top left), vertical effective stress (top right) and horizontal (bottom right) evolution with time. Bottom left: stress state projection in  $(-p', q)$  for isothermal and THM simulations for the first seal rock element.**

The injection of cold  $\text{CO}_2$  will lead to a contraction of subsurface rock due to its cooling effect and then will tend to decrease the observed surface displacement compared to the isothermal case (Figures 26 and 27).

## Earth Sciences and Environmental Technologies Division

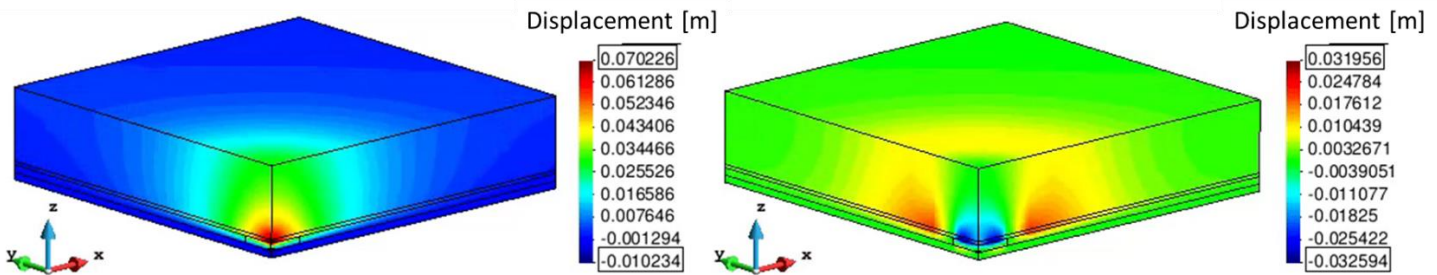


**Figure 26 : Vertical displacement [m] after one year of injection for the isothermal case (left) and THM case (right) [note: not the same color scale for both pictures].**

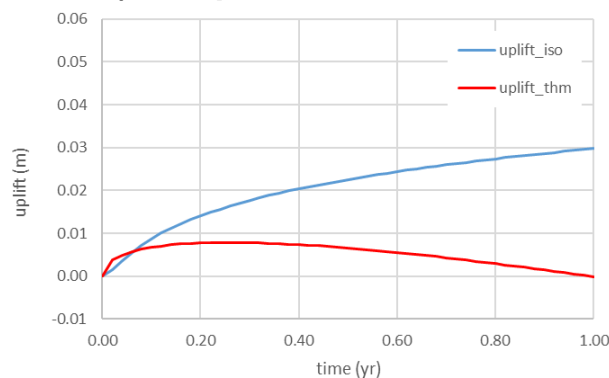


**Figure 27 : Comparison between isothermal and THM simulations results for the surface displacement (on top of the injection point).**

The THM simulation must be analyzed with caution (high injection rate, exaggerated temperature decrease, monophasic fluid...), nonetheless, the following behavior may be expected when injecting cold CO<sub>2</sub> in subsurface:

- Contracting deformation tendency due to rock cooling
- Horizontal effective stresses increase and potential risk of rock failure depending on the considered initial stress state

The study has been performed for a single set of parameters. It may provide some insights about the reservoir physics, but additional sets of parameters could be investigated.



### 4 Ground surface response analysis to CO<sub>2</sub> leakage through a fractured zone above the injection interval

In this section, we analyze the ground surface response to the opening of a fracture zone located above a CO<sub>2</sub> injection interval. More precisely, our objective is to identify what parameters and how they control the ground surface response to this fracture opening, by analyzing numerical simulations of CO<sub>2</sub> injection experiments in a synthetic model.

We first describe the design of the reference model in which the ground surface response shows a displacement pattern controlled by the fracture zone, according to the displacement pattern observed above injection well KB-502 of the In Salah injection experiment in Algeria (Rinaldi and Rutqvist, 2013). Then, results of a sensitivity analysis to the different model's parameters are examined.

#### 4.1 Synthetic Model

The structural model chosen for this study was derived from the “Sandstone I” model developed in WP 2.1 (see Deliverables 2.1 and 2.2, Bouquet et al. 2021). Its design is inspired from the In Salah project where a fracture zone opening (or re-opening) was observed during a CO<sub>2</sub> injection experiment.

Properties of this synthetic test case are reported in Deliverable D2.1. The dimension of the model is 60 km X 60 km with a total thickness of 2200 m. It is made of four structural layers, from bottom to top: the underburden, the reservoir, the overburden and the caprock. The latter is supposed to be impervious and is considered as a no-flow zone in the fluid flow simulations (Figure 28).

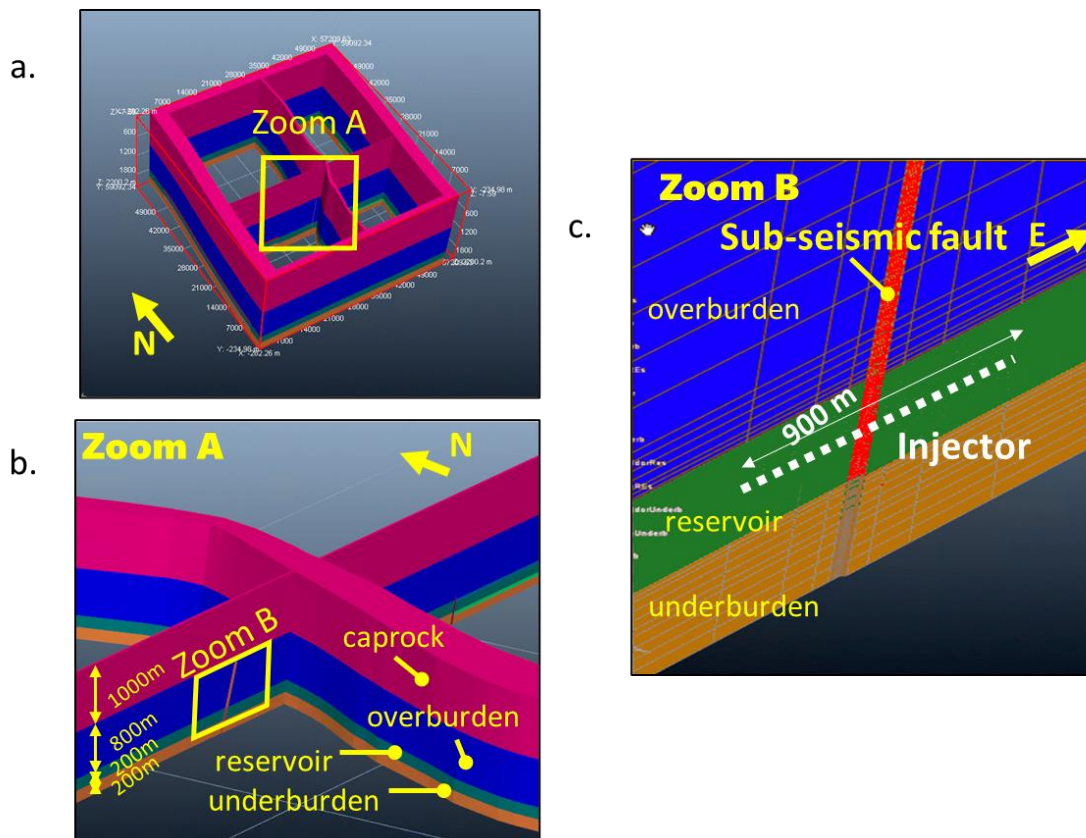


Figure 28 : Presentation of the reference synthetic model

## Earth Sciences and Environmental Technologies Division

The model structure includes a 45 m high anticline, two seismic faults and one sub-seismic fault with a 10 m maximum throw. The sub-seismic fault is located on the flank of the anticline, as shown on Figure 29. In this study, the seismic faults were not considered as hydrodynamic discontinuities and the rock properties values in the damage zone and the core of these faults are identical to that of the reservoir.

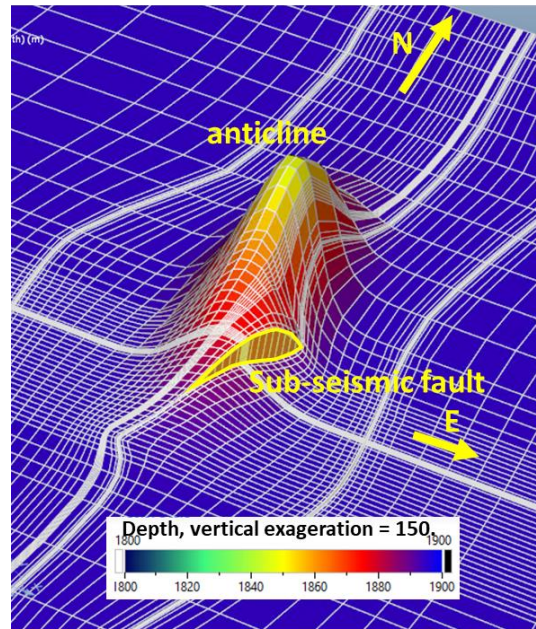


Figure 29 : Zoom on the anticline and the sub-seismic fault, top reservoir layer

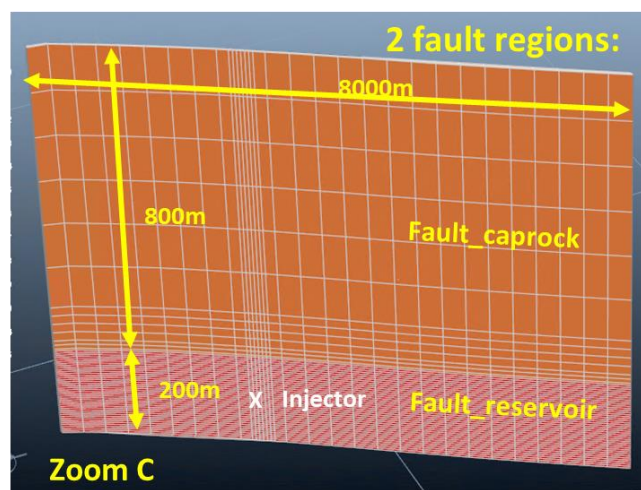
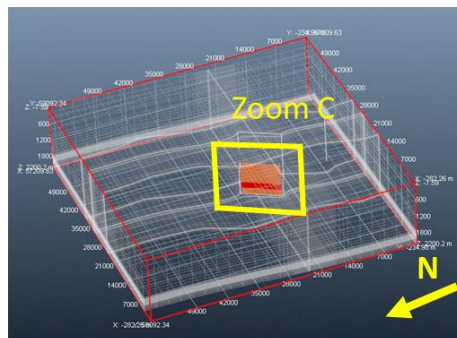


Figure 30 : Geometric properties of the sub-seismic fault

## Earth Sciences and Environmental Technologies Division

The sub-seismic fault is located at the center of the model (Figure 30). It is 8000 m length, 60 m thick and 1200 m high. It dips to the west, trends to the north-east and extends vertically from the reservoir base to the top of the overburden. It is split in a reservoir region and an overburden region, as shown on Figure 30.

The underburden is discretized with 10 layers, the reservoir is discretized with 40 thin layers, the overburden is discretized with 14 layers. Horizontal cell sizes vary from 20 m to 3500 m, with local grid refinement to precisely model faults.

### 4.2 Coupled hydro-mechanical simulator

Hydrodynamical and geo-mechanical response to CO<sub>2</sub> injection is simulated with a coupled flow-geomechanics simulator described in Deliverable D2.2, section 2.1.

The coupled hydro-mechanical simulator shows several limitations which need to be noted here:

- Since all simulations are run here in one-way coupling, no direct retroaction of mechanical calculation on flow properties are applied (*i.e.*, no change in porosity or permeability from mechanical simulation).
- Only one episode of permeability change can be prescribed during a flow simulation. The date of the permeability change must be prescribed by the user, as well as the amplitude of the permeability change which can be defined cell by cell.
- Only a relationship between permeability and absolute pressure can be defined (it is not possible to prescribe a permeability-vs- $\Delta P$  relationship where  $\Delta P$  is the overpressure developed since the beginning of the injection).
- Rock compressibility is a static data (constant value per zone) in the reservoir simulator.
- Elastic parameters of the rock are isotropic in the mechanical simulator.

A consequence of these limitations is that we can only simulate an instantaneous fracture opening episode, which must be pre-defined in terms of permeability change and fracture zone. In other words, slow propagation of fracture opening under the effect of pressure increase cannot be modeled.

All simulations presented below are run in one-way coupling.

### 4.3 The reference scenario

#### 4.3.1 Model parameters:

The reference scenario was designed with the constraint that a double-lobe displacement pattern as close as possible to the displacement pattern observed in the In Salah experiment can be observed, while keeping as much as possible the parameters of the synthetic "Sandstone I" model from WP 2.1.

The injection well was placed horizontally in the model, so that the sub-seismic fault hits the injection segment in its center. It was placed 100 m below the reservoir-overburden interface. Its length was set to 900 m. The injection rate was set to  $1.5 \cdot 10^6$  m<sup>3</sup>/day at surface conditions, to obtain a pressure increase in the injection well which fits approximatively to the pressure increase observed in the In-Salah experiment. This injection flowrate was kept constant throughout the simulations.

All parameters of the sub-seismic fault were prescribed to be uniform within each region. Fracture opening was supposed to occur 275 days after the injection start, and the calculation simulated 475 more days so that a little more than a two-years experiment is simulated.

The reference scenario was obtained by a manual trial and error process, by adjusting permeability and compressibility of the two regions of the sub-seismic fault after fractured opening. In the reference model finally

## Earth Sciences and Environmental Technologies Division

selected, only the overburden region of the sub-seismic fault was supposed to experiment fracture opening (or re-opening), and the reservoir region was modelled with the same properties as the reservoir itself.

The rock parameters of the reference scenario are summarized in table 5.

**Table 5 : Rock properties values for the reference scenario**

	Porosity [-]	Permeability [mD]	Compressibility <sup>3</sup> [bar <sup>-1</sup> ]	Poisson ratio [-]	Young's modulus [Pa]
<b>Overburden</b>	5%	0.001 mD	0.0000443	0.25	6.77E+10
<b>Reservoir</b>	10%	2 mD	0.0000265	0.25	5.66E+10
<b>Underburden</b>	10%	0.001 mD	0.0000443	0.25	3.39E+10
<b>Caprock</b>	0	0		0.25	1.00E+10
<b>Sub-seismic fault, overburden region</b>	5%	<b>0.001 mD, 0.3 mD</b>	0.001	0.25	6.00E+08
<b>Sub-seismic fault, reservoir region</b>	10%	2 mD	0.001	0.25	6.00E+08

### 4.3.2 Reference scenario results

The experiment is split in two phases, before and after fault opening. Simulation results of the reference scenario are presented in Figures 31 to 42.

#### Phase I

During the first phase of the experiment, before fracture opening, the injection is responsible of a maximum ground uplift of 8 mm. A map of the calculated uplift and an EW profile of the ground surface vertical displacement at the end of this first phase are presented in Figure 31 and Figure 32.

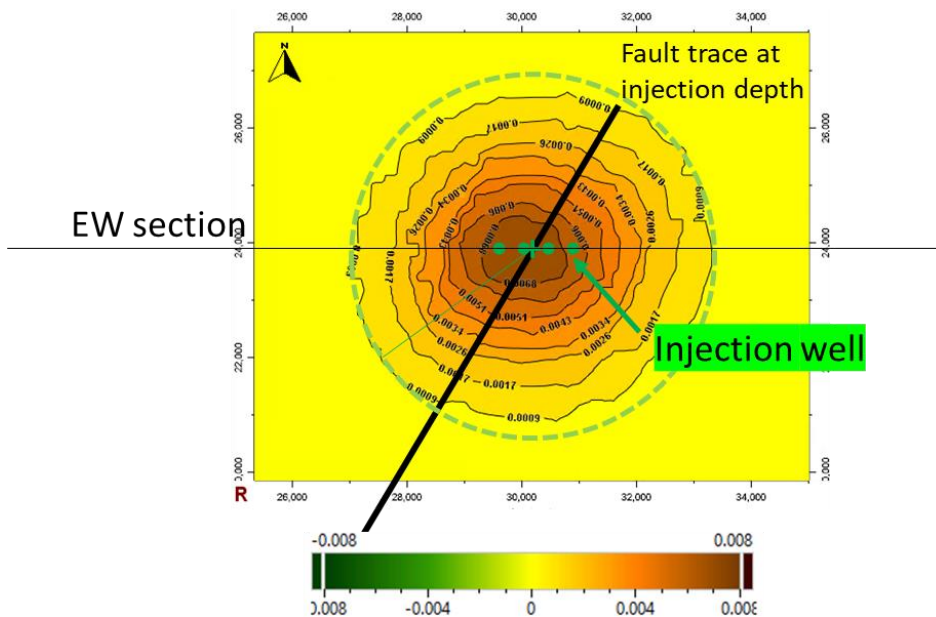


**Figure 31 : Ground vertical displacement [m], at time t=275 days (i.e., phase 1, just before fracture opening) in the reference experiment. The green dashed line is a reference circle with a radius of 3200m.**

$$^3 Cp = \frac{1}{\phi} \left( \frac{3(1-2\nu)}{E} \right)$$

## Earth Sciences and Environmental Technologies Division

### Ground displacement since injection start

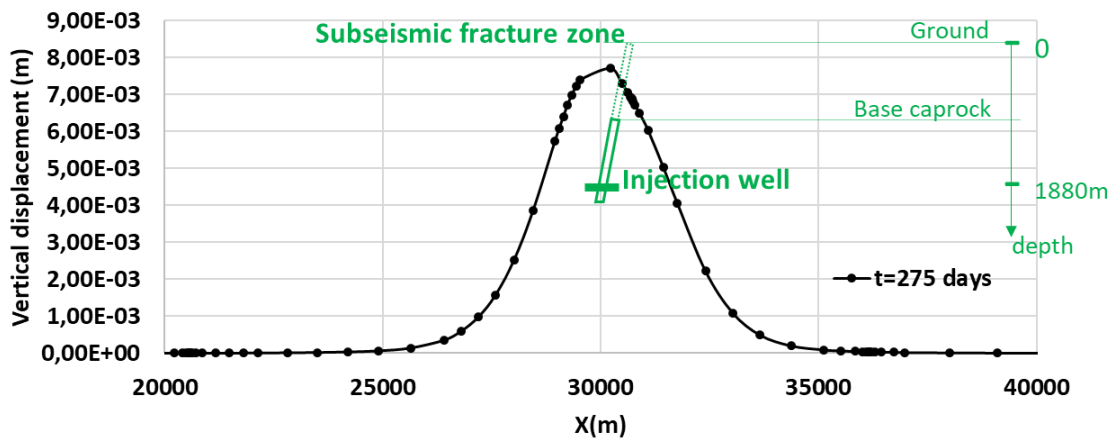


**Figure 32 : EW section of the vertical component of the ground surface displacement in meters, before fracture opening, in the reference experiment**

The ground uplift is centered on the middle of the injection well and fault trace at reservoir depth (not centered on the fault trace projected at surface due to the fault dip). We also check that the fault does not disturb the displacement pattern before fracture opening, as expected.

### Phase II

Phase II of the experiment starts with the opening of the sub-seismic fault at time = 275 days. Fracture opening is simulated by increasing the permeability of the overburden region of the sub-seismic fault by a factor 100. Evolution with time of the well pressure is represented on Figure 33. Fracture opening creates a 5 MPa pressure decrease in the well, which is higher than the approximate 2 MPa pressure decrease observed in the In Salah experiment but remains in the same order of magnitude.

### Pressure evolution in the injection well

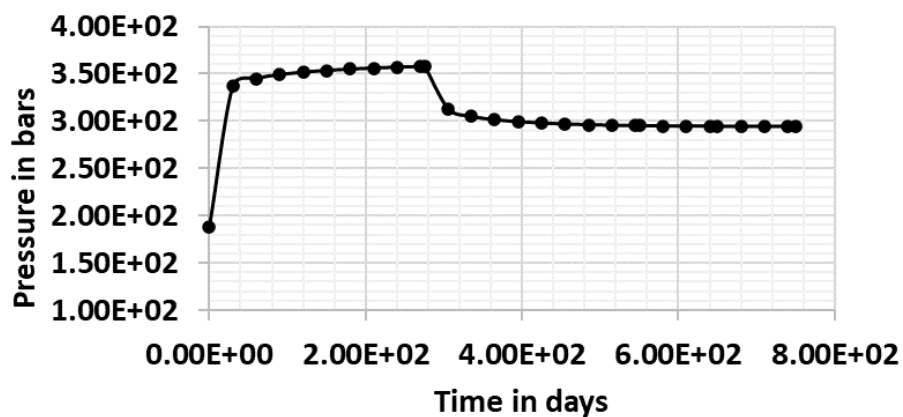
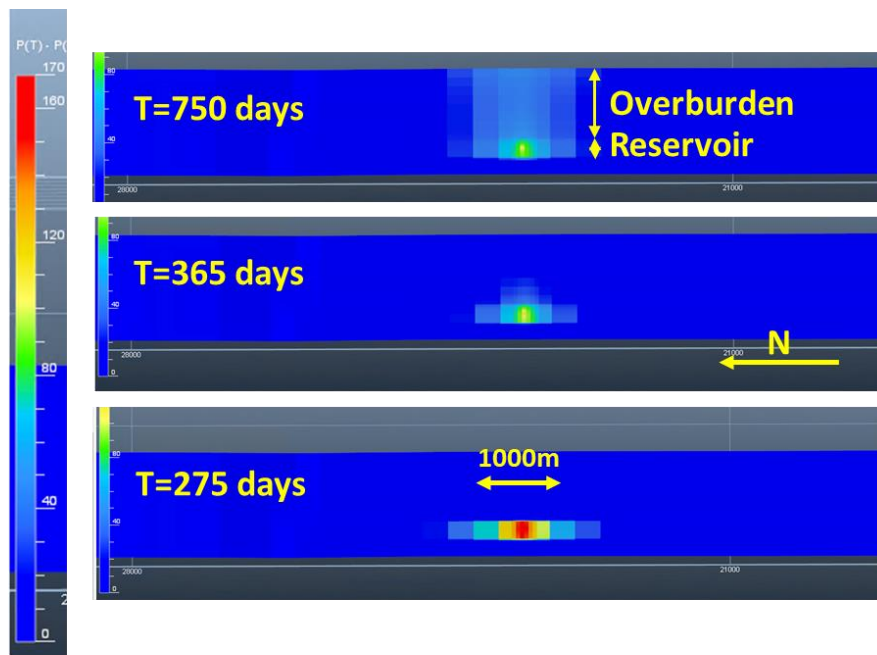


**Figure 33 : Evolution of well pressure at the middle of the injection well, during the reference experiment**

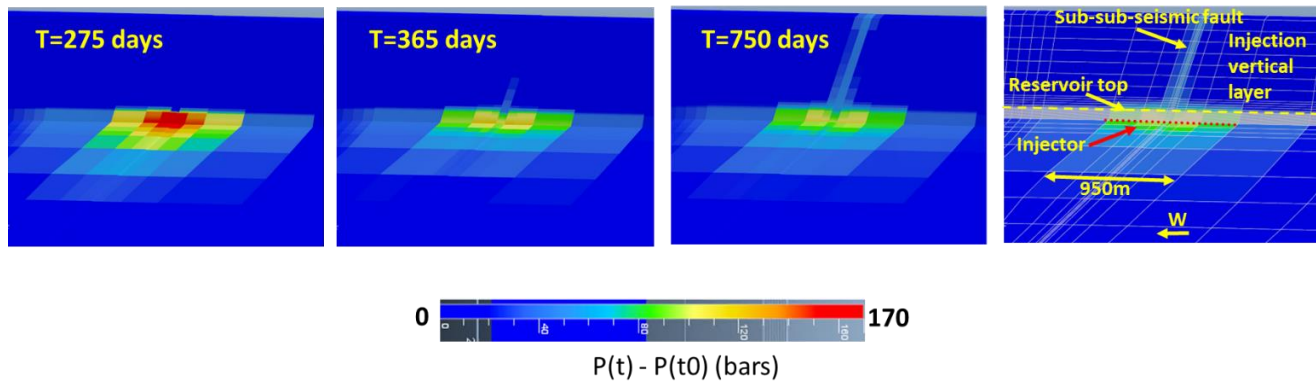
Pressure evolution through time inside and across the sub-seismic fault plane are represented in Figures 33, 34 and 35. The overpressure is strictly limited vertically to the reservoir top and bottom before fracture opening. After fracture opening, maximum pressure decreases in the reservoir, but the overpressure plume starts to extend slowly upwards, in the overburden region of the fault.

## Earth Sciences and Environmental Technologies Division



$P(t) - P(t_0)$  (bars)

Figure 34 : Pressure evolution through time inside the sub-seismic fault surface, in the reference experiment



$P(t) - P(t_0)$  (bars)

Figure 35 : Pressure evolution through time across the sub-seismic fault surface, in the reference experiment. The vertical and horizontal planes used for the visualization intersect each other along the injection well.

Total vertical displacements of the ground surface during all the injection period (all the simulation) and during phase II are presented in Figures 36 to Figure 40.

## Earth Sciences and Environmental Technologies Division

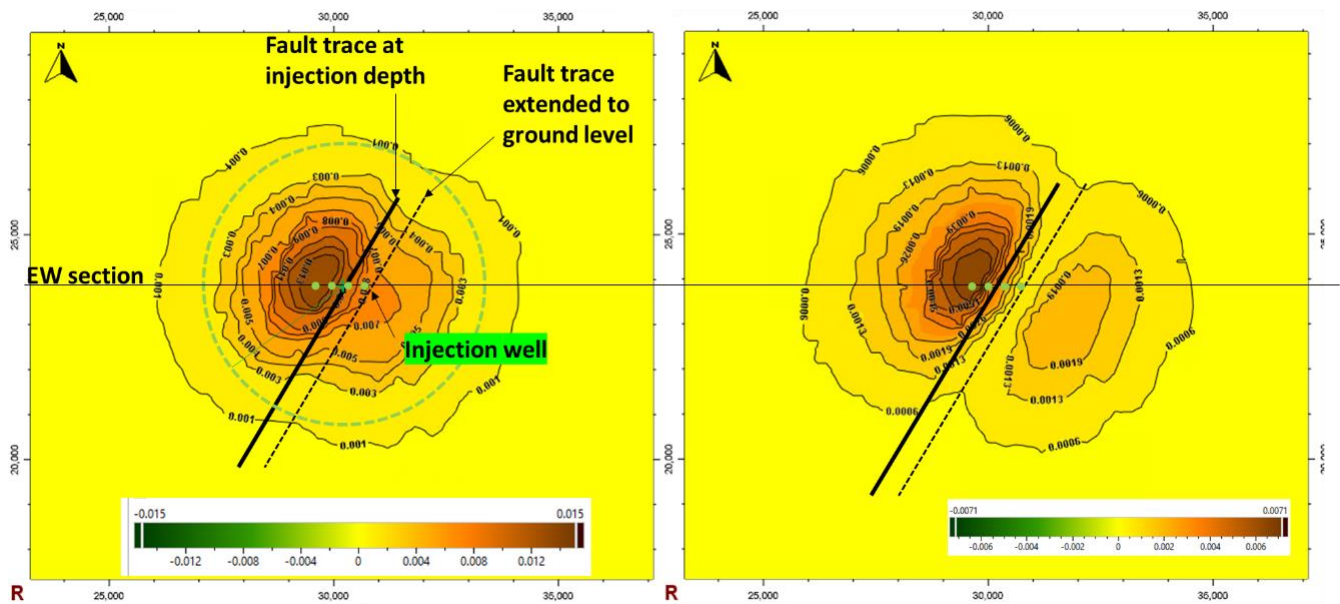


Figure 36 : Map of the total vertical displacement [m] of the ground surface. Left: during all the injection period. Right: during phase II. The green dashed line is the reference circle from Figure 31.

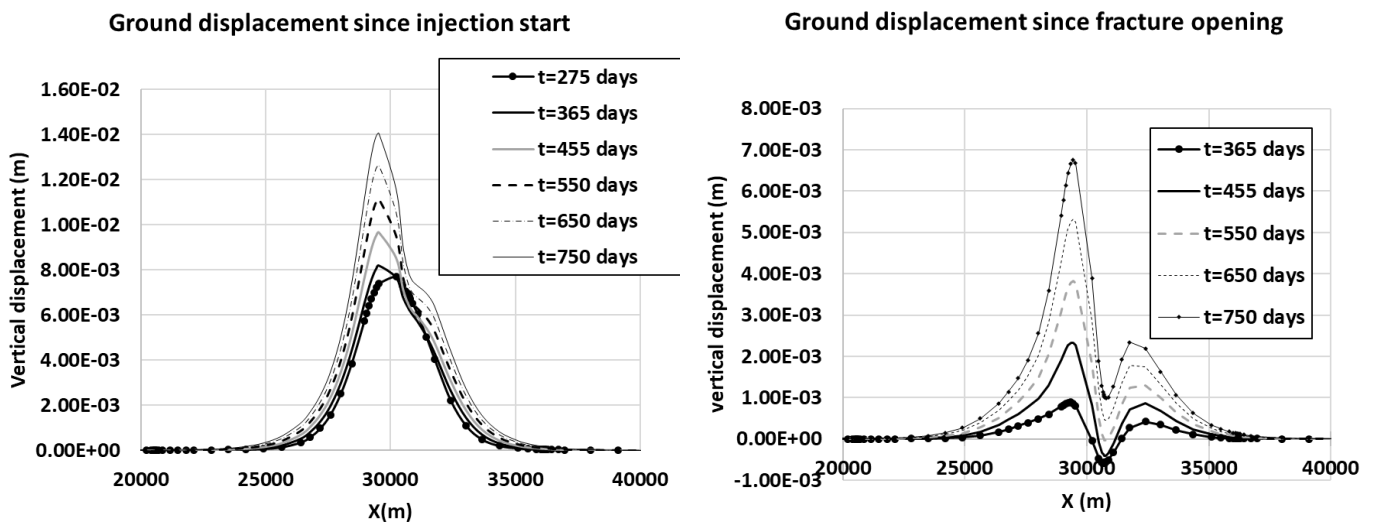
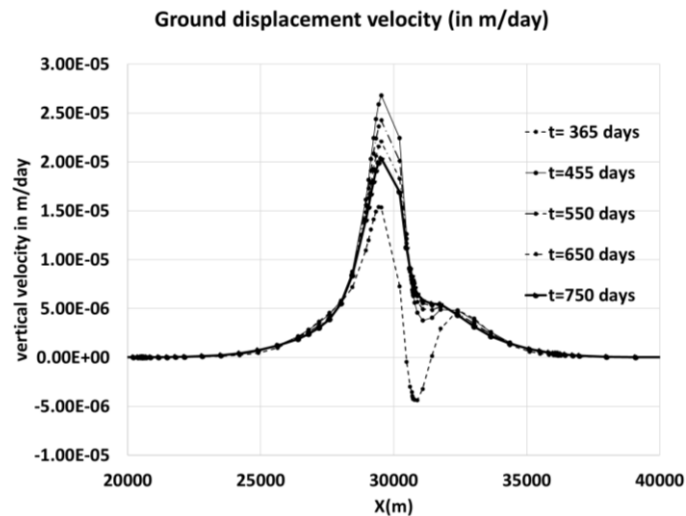


Figure 37 : EW cross-sections of the vertical ground surface displacement in the reference experiment. Left: during all the injection period. Right: during phase II.

Three months after fracture opening, at time  $t=365$  days, a 0.6 mm subsidence can be observed above the fault trace (Figure 37), and 2 areas of uplift appear on both sides of the fault trace, with a maximum uplift located about 1.5 km from the fault (Figure 36). The uplift lobes are not symmetrical as the uplift amplitude to the west of the fault is 0.8 mm while it is 0.4 mm to the east. The difference observed between the two lobes is mostly due to the fault dip (see Figure 39 and comments).

Twelve months after fracture opening, all the area perturbed by the injection is uplifted even above the fault trace, but uplift velocity above the fault trace is lower than the uplift velocity of the uplifted area to the west (Figure 38). The maximum uplift velocity is observed on the lobe to the west at time  $t=455$  days, *i.e.*, 6 months after fracture re-opening. Then, the uplift velocity to the west of the fault starts to decrease.

## Earth Sciences and Environmental Technologies Division



**Figure 38 : Ground surface displacement velocity along the EW profile at different times, in the reference experiment.**

At the end of the simulation, *i.e.* 15 months after fracture opening, the total vertical displacement pattern is visibly modified by the fault opening (Figure 37, left), but the relatively low uplift above the fault trace is not yet sufficient to reproduce two distinct uplift lobes, as those observed in Salah. However, Figure 37 (right) which represents the cumulated displacement after the opening clearly shows a two-lobes structure controlled by the sub-seismic fault. Results obtained from this synthetic model are qualitatively comparable to those obtained from InSAR measurements at In Salah site, see for example Figure 50 reproduced from Rinaldi and Rutqvist, 2013.

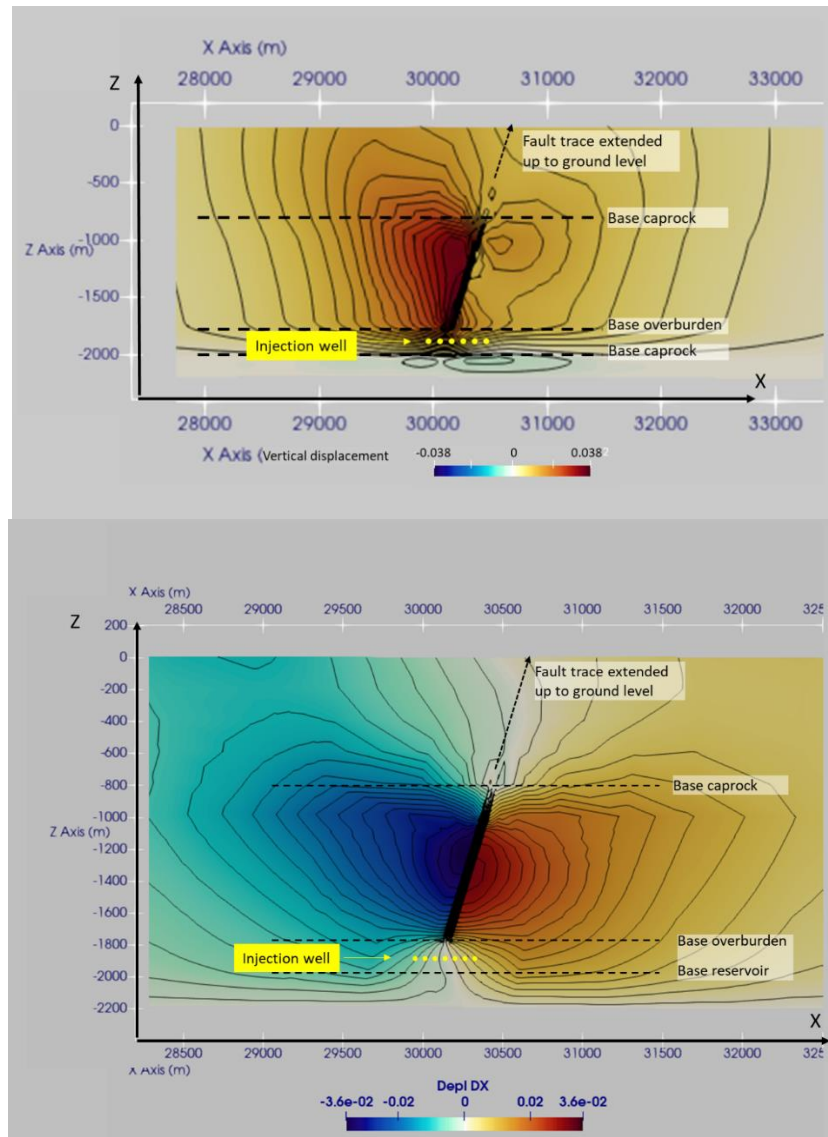
During all the experiment, the uplift velocity above the fault trace is much lower than the uplift velocity of the lobe to the west and lower or equivalent to the uplift velocity of the lobe to the east, meaning that the relative uplifting of the lobe to the west is still ongoing at the end of the experiment.

Figure 39 shows the spatial distribution of the displacement in X and Z directions along the vertical EW cross-section including the injection well. The largest displacements are observed in the overburden, against the western wall of the sub-seismic fault. The displacement in the overburden is mitigated by the stiff caprock, leading to maximum vertical displacement of the ground surface of about 8 mm, while it reaches 38 mm in the overburden. The analysis of the displacements in the EW direction shows a cumulated opening of the sub-seismic fault reaching 7 cm, with the largest opening located in the center of the fault.

Figure 39 shows that the fault plane splits the model in two blocks regarding to X and Z displacements: the upper fault compartment where high vertical displacements are concentrated against the fault and mitigated by the caprock, and the lower compartment where much smaller vertical displacements can be observed. We note that the normal to the fault in the upper compartment intersects a free surface (the ground), while the normal to the fault in the lower compartment intersects a fixed boundary (the base of the model). This might explain the differences between the two lobes in terms of vertical displacement: the free surface promotes vertical displacement in the upper compartment, while the bottom boundary prevents vertical displacements in the lower compartment.



## Earth Sciences and Environmental Technologies Division



**Figure 39 : EW vertical cross-section of the total displacement field in meters in the Z direction (Top) and X direction (Bottom), for all the injection period.**

In Figure 40, we compare the uplift profile of the reference simulation to the profile obtained in the same system, but without fault opening: the maximum observed uplift after 15 months is the same in both simulations, but the relative subsidence created by the fault is clearly observable in the reference experiment.

## Earth Sciences and Environmental Technologies Division

Ground displacement since injection start

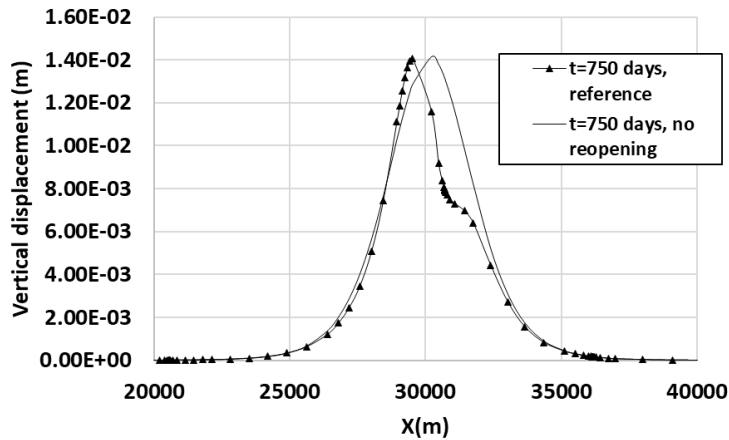


Figure 40 : EW cross-section of the total vertical displacement profiles of the reference experiment (curve with symbols) and of the same experiment but without fracture opening (curve without symbol) at t=750 days.

Finally, gas saturation along and across the sub-seismic fault are presented in Figure 41 and 42. After fracture opening, gas migrates slowly upwards inside the overburden region of the fault. 15 months after fracture opening, gas has leaked up to the top of the overburden region of the sub-seismic fault along a 2.5 km distance, with a CO<sub>2</sub> saturation above 20%.

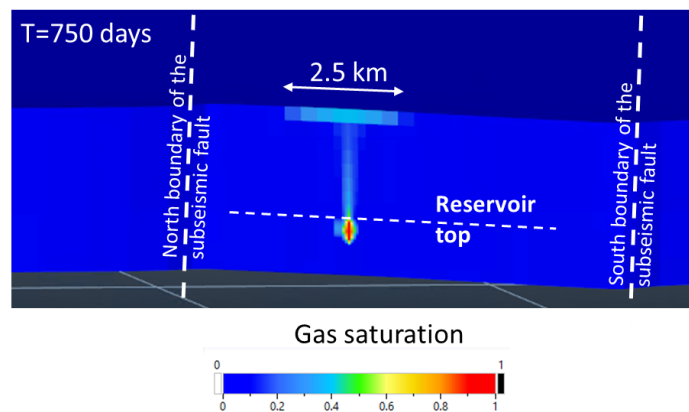


Figure 41 : Gas saturation inside the opened sub-seismic fault surface, at the end of the reference experiment

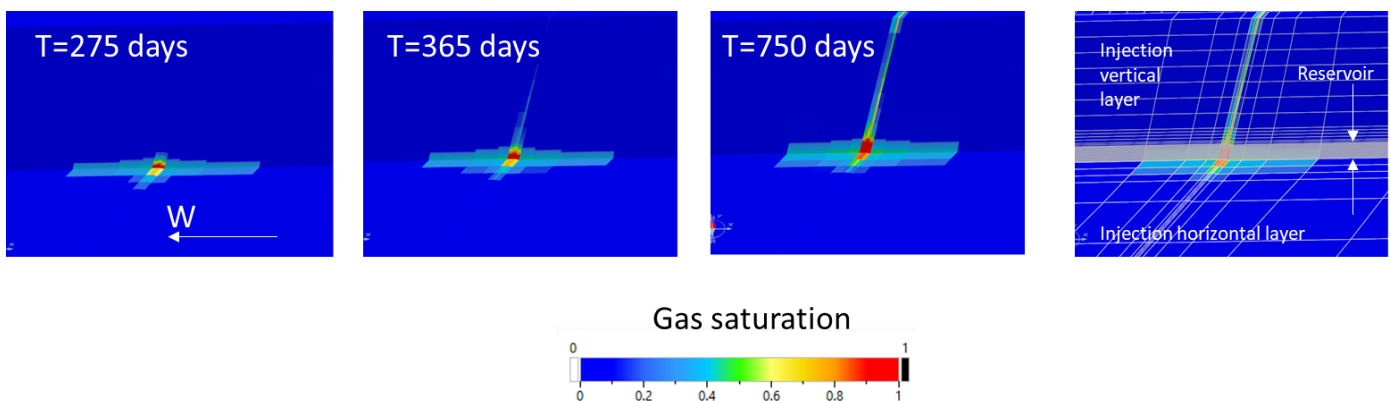


Figure 42 : Gas saturation along 2 planes, horizontal and vertical, across the sub-seismic fault and along the injection well, at times t=275 days, t=365 days and t=750 days. Image on the right visualize the discretization and the position of the planes used for the visualization.

## Earth Sciences and Environmental Technologies Division

### 4.3.3 Conclusion on the reference case

Only the displacement pattern of the ground surface after fracture opening (Figure 36) shows a clear two-lobes pattern. However, the total displacement pattern (Figure 37) is visibly controlled by the fault opening with a lower uplift above the fault trace, creating a local constriction of the uplifted area.

We will see in the next section that a more pronounced relative subsidence above the fault lineament could have been obtained with a higher permeability increase or a higher fault compressibility, but this would have increased the pressure drop observed at fracture opening which is already quite high if we compare it to the pressure drop observed in In Salah.

In this reference case, the visible modification of the ground displacement profile by the sub-seismic fault opening is obtained by multiplying the permeability of the overburden region of the fault after opening by a factor 100, and assuming a compressibility of the fault which is about 20 to 25 times larger than the overburden compressibility. With these parameter settings, the sub-seismic fault width increases by a maximum of 7 cm after opening, for a total width of 60 m. This makes the CO<sub>2</sub> plume propagate inside the fault plane to the top of the overburden region of the fault. The length of the CO<sub>2</sub> plume inside the fault plane reaches 2.5 km at the end of the experiment (18 months after the opening).

## 4.4 Sensitivity Analysis

### 4.4.1 Sensitivity to fault length

Two alternative scenarii were analyzed, in which the sub-seismic fault is lowered from 8 km to 3.1 km and 2km long respectively. In both cases, the injection well hits the fault trace in its center.

The vertical ground displacement along the EW section from the reference scenario and from these two alternative scenarii are presented in Figure 43, at time t=365 days and t=750 days after injection start.

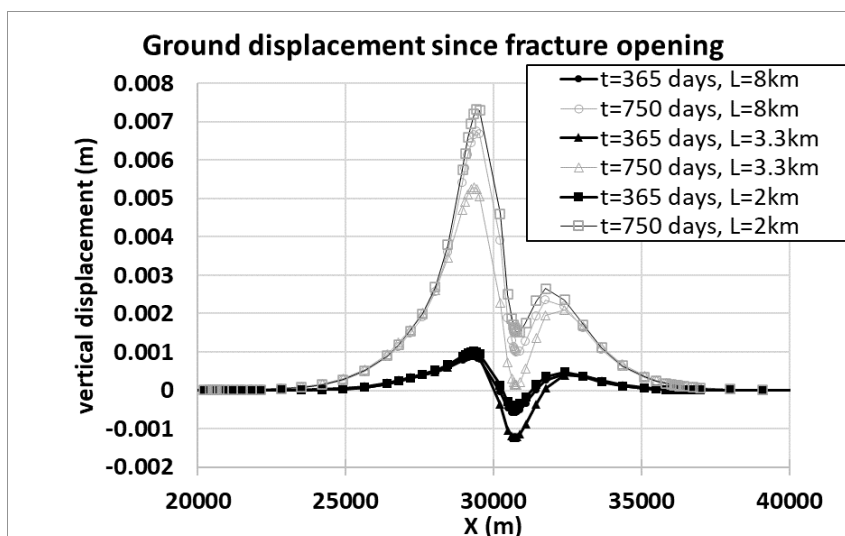


**Figure 43: EW vertical cross-section of the vertical ground displacement for 3 scenarii with varying fault lengths L=8km (reference experiment), L=3.3km and L=2km**

The largest subsidence is observed with a fault length of 3.3 km, and similar subsidence is observed for 2 km and 8 km fault lengths. Differences between these scenarii can be explained by the competition between the pore volume made accessible inside the fault and the pressure homogenization along the fault: the longer the fault, the higher the pore volume made accessible, but the higher pressure and displacement balancing along the horizontal direction. However, the 3 subsidence profiles remain quite similar. This can be explained with Figures 34 and 35, where we observe that the length of the overpressure area inside the fault region is very narrow (only 1.5 km)

## Earth Sciences and Environmental Technologies Division

compared to the fault length, meaning that the flow perturbation created by fault opening is very limited in space and located above the injector.

### 4.4.2 Sensitivity to the vertical position of the injection well

The reference scenario is compared here to a similar scenario where the injection well is 25 m from the top of the reservoir instead of 100 m, which is more in accordance with the In Salah experiment.

The vertical ground displacement along the EW section for these 2 scenarii is represented in Figure 44. The displacement patterns are very similar for the two scenarii, meaning that this parameter has very little control on the displacement pattern.

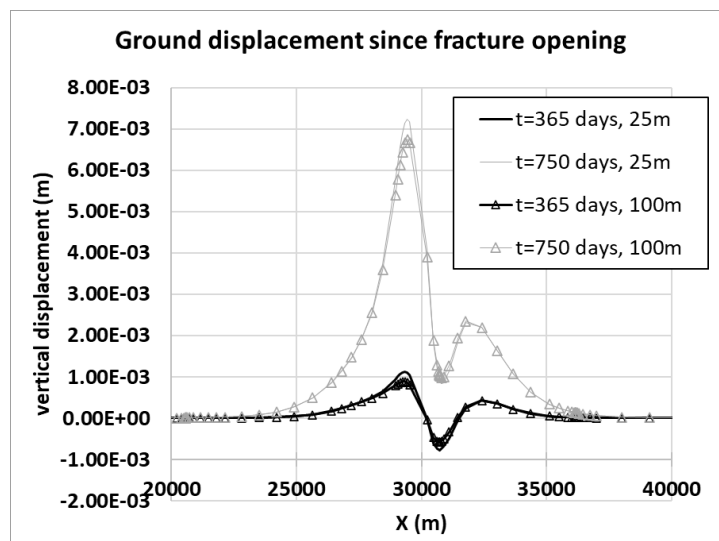
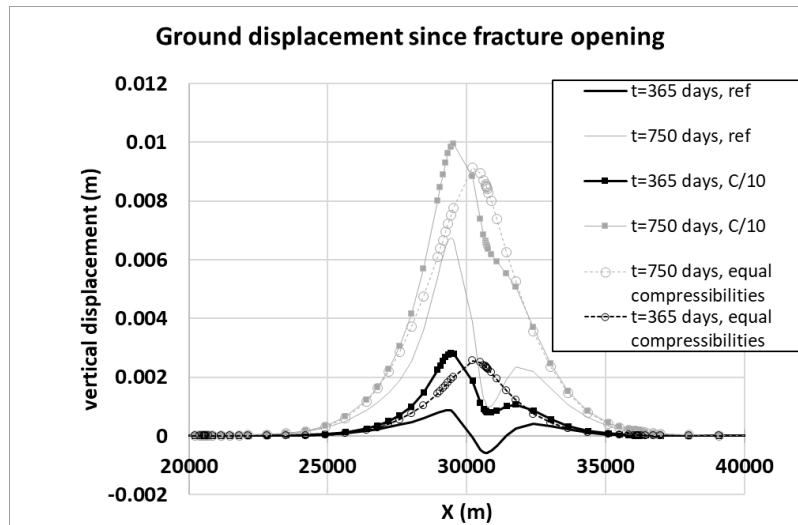


Figure 44 : EW cross-section of the vertical ground displacement for two distances between the injector and the reservoir top, L=100m and L=25m

### 4.4.3 Sensitivity to sub-seismic fault compressibility

Here, we analyze the sensitivity of the ground displacement pattern to the compressibility of the overburden region of the sub-seismic fault. The reference experiment is simulated with 3 different values of the fault compressibility in the overburden:  $C_p=1e-3 \text{ bar}^{-1}$ ,  $C_p=1.e-4 \text{ bar}^{-1}$  and  $C_p=4.43e-5 \text{ bar}^{-1}$ . In the case  $C_p=4.43e-5 \text{ bar}^{-1}$ , the overburden region of the fault has the same compressibility as the surrounding rock and the fault is only characterized by a permeability which differs from that of the overburden. The calculated displacement profiles are presented in Figure 45.

## Earth Sciences and Environmental Technologies Division



**Figure 45 : EW cross-section of the vertical ground displacement for 3 compressibility values of the overburden region of the sub-seismic fault: reference compressibility  $C_p=1.e-3 \text{ bar}^{-1}$ ,  $C_p=1.e-4 \text{ bar}^{-1}$ , and  $C_p=4.43 e-5 \text{ bar}^{-1}$**

The reference scenario and both alternative scenarios with lower fault compressibility show very different results. The reference scenario shows a well visible subsidence above the fault all along the experiment, while the scenario with a fault compressibility divided by 10 shows a moderate subsidence of the uplift profile 90 days after fracture opening, and almost no more visible subsidence at the end of the experiment. The scenario with equal compressibility values in the fault and in the surrounding rock is not perturbed by sub-seismic fault opening.

These results show that the control of the sub-seismic fault opening on the vertical ground uplift increases when the fault compressibility increases. This can be explained by the fact that the more compressible the fault, the greater the leakage of the pressurized area of the reservoir into the fault zone, thus making the reservoir depletion more important.

#### 4.4.4 Sensitivity to time of fracture opening

We analyze here a new scenario in which the fracture is opened as soon as the injection starts. We compare the result to the reference scenario and to a scenario in which the sub-seismic fault is not re-opened during injection (Figure 46).

The uplift profile with the sub-seismic fault opened at the beginning of the injection does not show any subsidence above the fault trace. Compared to the case without fault opening, the constant leak since injection start creates a small relative subsidence. This subsidence is well distributed along the section instead of being localized above the fault trace when the fracture is opened after 275 days. In other words, the leakage from the beginning of the injection would not be easily detectable from the analysis of the displacement pattern. Moreover, the maximum uplift amplitude is almost the same in all scenarios.

## Earth Sciences and Environmental Technologies Division

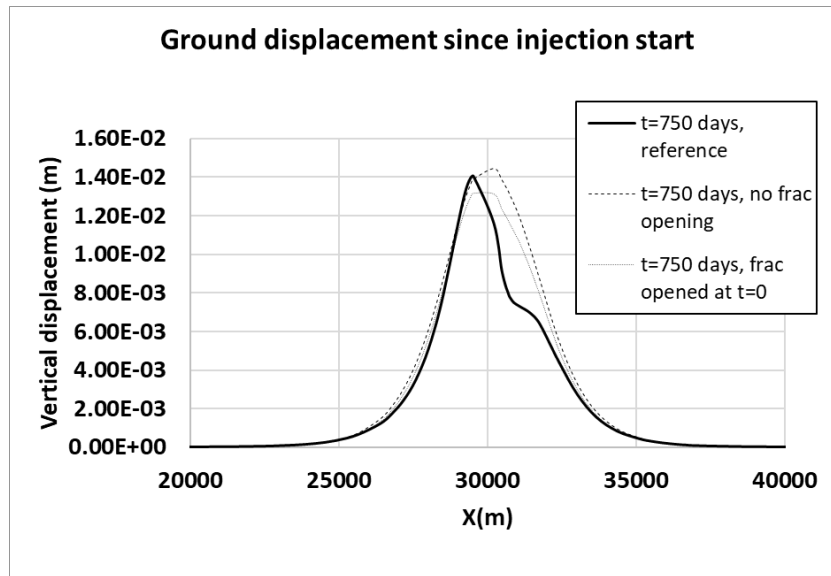


**Figure 46 :** EW cross-section of the vertical ground displacement at the end of 3 experiments: the reference one, an experiment with no sub-seismic fault opening and an experiment with sub-seismic fault opening as soon as injection starts.

### 4.4.5 Sensitivity to sub-seismic fault permeability increase at fracture reopening

We compare the reference scenario where permeability is multiplied by 100 at fracture opening with a new scenario where permeability is multiplied by 30. Although the permeability increase at fracture reopening is only 3.3 times smaller in this new scenario, the displacement profile is very different and shows a much smaller subsidence above the sub-seismic fault trace (Figure 47).

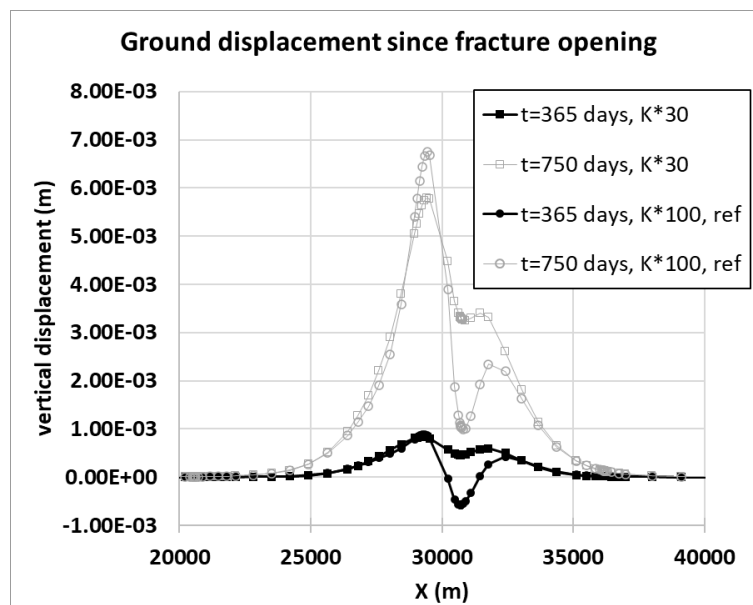


**Figure 47:** EW cross-section of the vertical ground displacement since fracture opening, for two experiments which differ in fault permeability increase at opening

When looking at the total vertical displacement since injection start of the two scenarii (Figure 48), it appears that the subsidence created by the leak is much more subtle in the case where the permeability is only multiplied by 30, making the leak almost undetectable from the analysis of the vertical ground displacement.

## Earth Sciences and Environmental Technologies Division

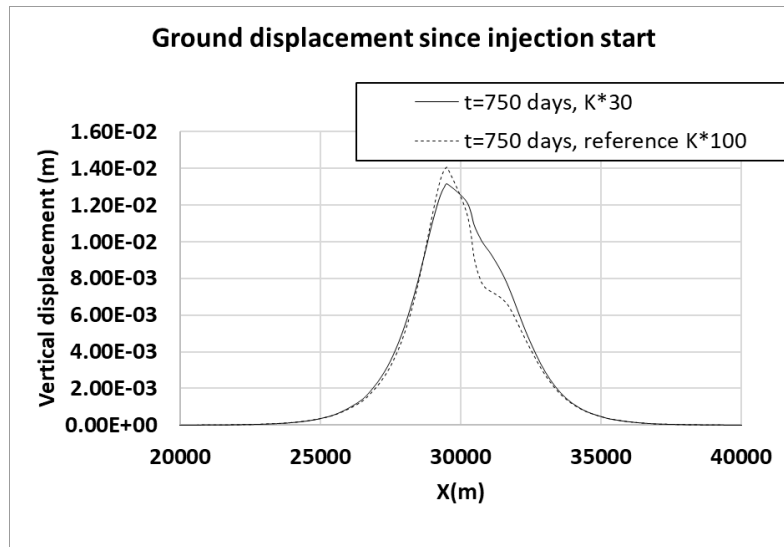


Figure 48: Comparison of the vertical displacement pattern on the EW cross-section since the beginning of the injection for two experiments which differ in fault permeability increase at opening.

### 4.4.6 Sensibility to overburden stiffness

Here we analyze how the caprock stiffness controls the ground surface response. In this alternative scenario, the caprock is 10 times softer than in the reference scenario. The comparison with the reference scenario is presented in Figure 49.

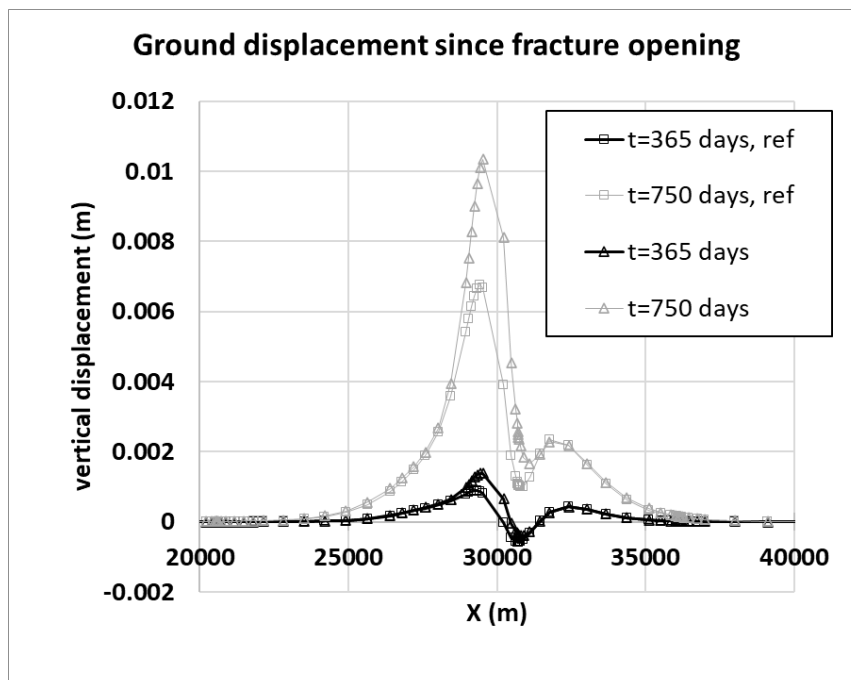


Figure 49 : EW cross-section of the vertical ground displacement for two experiments which differ in the caprock stiffness by a factor 10

The caprock stiffness has more control on the uplift lobe to the west of the fault than on the lobe to the east. The maximum uplift and thus the asymmetrical behavior is more pronounced with the softer caprock. This could be explained by a mechanical interaction with the anticline, since the caprock is thinned by 48m above the anticline,

## Earth Sciences and Environmental Technologies Division

which represents 5% of its total thickness. However, the fault dip could be the most contributing factor, as explained on Figure 39 and comments.

### 4.4.7 Conclusion about the sensitivity analysis

The characteristics of the subsidence created by a leakage through a fault of the caprock are very sensitive to several parameters:

- The fault compressibility and the permeability increase at fault opening are the most controlling parameter. For a permeability increase 3 times lower than in the reference case or for a fault compressibility 10 times lower, the subsidence above the fault is no more detectable. To make it simple, this can be explained as follows: fault compressibility controls the volume of fluid which can leak inside the fault (and indirectly the amplitude of the relative subsidence), and fault permeability controls the velocity of the leaking fluid (and indirectly the duration of observed relative subsidence). Fitting both amplitude and duration of the observed relative subsidence, which exceeds 1 year in the case of In Salah, needs to calibrate fault compressibility and fault permeability at the same time.
- Elapsed time between the injection start and the fault opening is also a determining parameter: if the leakage starts at the same time as the injection, its effect on the displacement profile is smoothed laterally, thus making the subsidence created by the leakage undetectable

On the contrary, some geometrical parameters of the system, like the fault length and the distance between the injection well and the interface between reservoir and caprock have only a low control on the vertical displacement pattern observed above the fault.



## 5 Summary and concluding remarks

The hydromechanical coupling detailed in Deliverable D2.2 has been extended to dual medium and Biot theory of poroelasticity. Several synthetic cases illustrate the impact of these upgrades, and several points are observed:

- The Biot theory of poroelasticity is more conservative as less displacement but more risk of failure are observed and should be prioritized in a risk assessment.
- The double medium scheme allows to work on a fractured medium. The results obtained are consistent with the single medium approach when the fracture density is low. The impact of fractures on the elastic properties is very strong and greatly impact observed surface displacement, but the homogenization approach used depends on poorly characterized parameters such as shape factor and fracture porosity.
- Thermal effects can significantly impact the near-well behavior and as such, should be considered in a risk analysis.

However, some functionalities appear to be missing in the dual medium scheme, mainly in the iterative coupling scheme: the retroaction on permeability values related to the increase in fracture density should be addressed since it could be crucial for cases like In Salah one as it was underlined in the second part of this report (see below).

In a second part, a synthetic model of CO<sub>2</sub> injection and caprock leakage has been built to reproduce the observations made on KB502 well in In Salah, at least qualitatively, in terms of pressure drop and vertical displacement pattern of the ground. The relative subsidence above the fault lineament has been obtained by simulating the opening of a sub-seismic fault in the overburden, just above the injection interval. The fault was modeled by a 60 m wide and 8 km long region of the overburden which is characterized by a compressibility 25 times larger than that of the surrounding overburden rock. Fracture opening was simulated by suddenly increasing the fault permeability by a factor 100, 275 days after injection start. All hydrodynamic and geomechanical rock parameters were kept isotropic.

A sensitivity study showed that the vertical displacement pattern of the ground is very sensitive to the leakage parameters, i.e., fault compressibility and fault permeability increase. Only a very narrow range of these two parameters can yield to a ground displacement pattern and pressure drop in agreement with those observed in In Salah. Also, no observable relative subsidence is observed with the calibrated parameters if the fault is opened as soon as injection starts.

Finally, we could observe that the CO<sub>2</sub> plume expands inside the fault and progressively migrates vertically up to the top of the fault and laterally up to 1.3 km away from the injector, 18 months after fracture opening.

These results were obtained with a simple model where mechanical properties are supposed to be isotropic and only the overburden region of the fault is supposed to be opened (contrary to the work presented by Rinaldi and Rutqvist, 2013) and where fault permeability was controlled “manually” instead of being controlled by pressure like in Bjornara et al, 2018, or Morris et al, 2011. Despite these simplifications, our synthetic model shows a relative subsidence above the fault which is qualitatively and somehow quantitatively like the observations at KB502 well at In Salah. However, it should be noted that the fitted fault permeability after opening is 20 times smaller than the reservoir permeability in our work while it is about 12 times larger in Rinaldi and Rutqvist (2013) despite comparable structures and material parameters, which should deserve to be further inquired. A possible explanation for the discrepancy between these two models is the dynamic of permeability changes assigned to the reservoir in Rinaldi and Rutqvist (2013). This leads us to the last remark below.

Complementary work could aim at improving the physical model, for instance by controlling fault permeability by pressure. We expect that a more complex but more physical model of interaction between pressure and fracture permeability could lead to quite different results: for instance, gradual fault opening could smooth the response of the system, thus decreasing the amplitude of the relative subsidence above the fault and changing the dynamics of the system, which would require to reconsider our calibrated scenario.

## Bibliography

Abousleiman, Y. and Nguyen, V., 2005. Poromechanics Response of Inclined Wellbore Geometry in Fractured Porous Media, *Journal of Engineering Mechanics*, Volume 131 Issue 11.

Bouquet, S., Estublier, A., Fournon A., Frey J., Malinouskaya I., 2021. Assuring integrity of CO<sub>2</sub> storage sites through ground surface monitoring (SENSE) – WP2.1: Presentation of conceptual models (Deliverable D2.1). SENSE report, Report D2.1, 19 p.

Bouquet, S., Estublier, A., Fournon A., Frey J., Malinouskaya I., 2021. Assuring integrity of CO<sub>2</sub> storage sites through ground surface monitoring (SENSE) - WP2.2: Understanding the mechanism of surface movement (Deliverable D2.2). SENSE report, Report D2.2, 89 p.

Bjornara, T.I., Bohli, B., Joonsang, P., 2018. « Field-data analysis and hydromechanical modeling of CO<sub>2</sub> storage at InSalah, Algeria », *International Journal of Greenhouse gas control* 79, 61-72

Coussy, O., 2004. Poromechanics. Chichester: John Wiley & Sons Ltd

Deflandre, J-P., Estublier, A., Baroni, A., Daniel, J-M., Adjémian, F., 2011. In Salah CO<sub>2</sub> injection modeling: A preliminary approach to predict short term reservoir behavior. *Energy Procedia*, Volume 4, Pages 3574-3581, <https://doi.org/10.1016/j.egypro.2011.02.286>

Mori, T., Tanaka, K., 1973. Average stress in a matrix and average elastic energy of materials with misfitting inclusions. *Acta Metall. Mater.* 42 (7), 597–629.

Ho, C K. 2000. "Dual Porosity vs. Dual Permeability Models of Matrix Diffusion in Fractured Rock". United States. <https://www.osti.gov/servlets/purl/763324>.

IFP Energies nouvelles (2018). PumaFlow 10.0 reference manual. France.

Morris, J.P., Haob, Y., Foxall, W., McNabb, W., "A study of injection-induced mechanical deformation at the In Salah CO<sub>2</sub> storage project", *International Journal of Greenhouse Gas Control*, 5 (2011) 270–280

Rinaldi, A.P., Rutqvist, J., 2013. Modeling of deep fracture zone opening and transient ground surface uplift at KB-502 CO<sub>2</sub> injection well, In Salah, Algeria. *International Journal of Greenhouse Gas Control*, 12 155–167.

Warren, J.E., and P.J. Root. "The Behavior of Naturally Fractured Reservoirs." *SPE J.* 3 (1963): 245–255. doi: <https://doi.org/10.2118/426-PA>.

White, J., Chiamonte, L., Ezzedine, S., Foxall, W., Hao, Y., Ramirez, A., McNab, W., 2013. Geomechanical behavior of the reservoir and caprock system at the In Salah CO<sub>2</sub> storage project. *Proceedings of the National Academy of Sciences*, doi: 10.1073/pnas.1316465111.

### Annex A - Tables

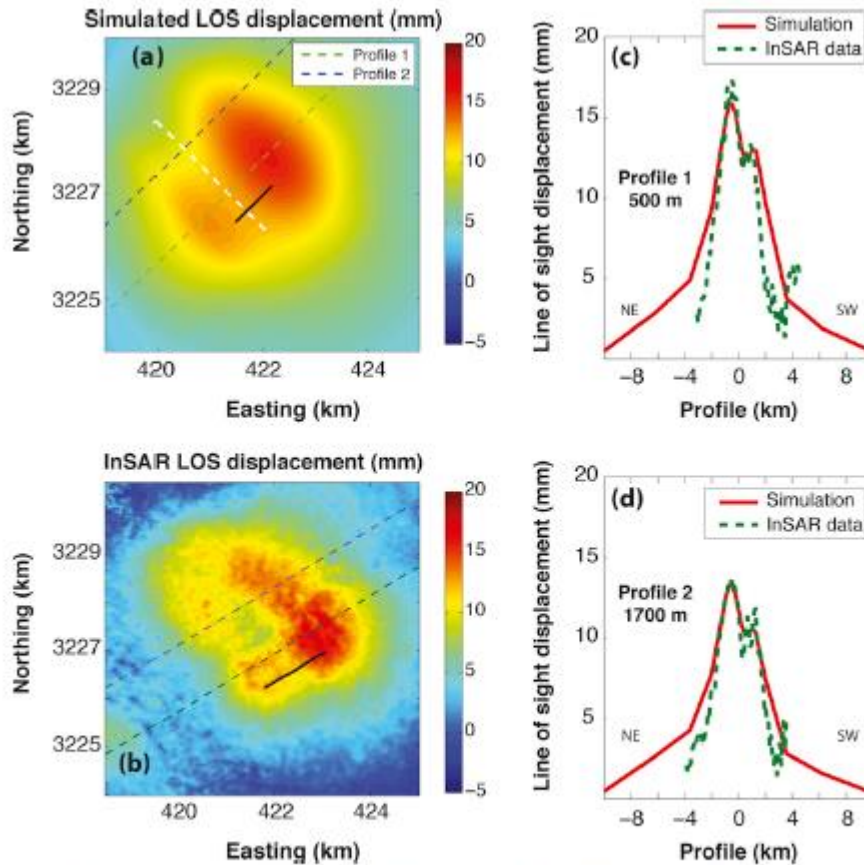
#### 1. Figures table

Figure 1 : Geometric description of the single-porosity porous medium (Coussy, 2004) .....	5
Figure 2 : Representation of the dual porosity medium for fractured rock (Abovsleiman and Nguyen, 2005).....	7
Figure 3 : Schematic description of the superposition of three continuous media (skeleton, porous and fracture) .....	7
Figure 4 : Schematic illustration of crack for considered fractured porous media .....	8
Figure 5 : Left, schematic representation of the dual-medium concept after Warrant and Root (1963). Illustration of the superposed mesh for representing the dual-medium with the flow simulator, PumaFlow (IFP Energies Nouvelles, 2018). .....	10
Figure 6 : From Ho (2000), illustration of two alternative conceptual models for matrix diffusion in fractured rocks: either no flow between matrix blocks (i.e., only matrix-fracture flow) or flow is allowed in both media. ....	10
Figure 7 : Homogenized Young Modulus and Poisson coefficient for dual-medium, function of skeleton shear and bulk moduli (top) and function of fracture porosity and shape factor (bottom). Inadmissible values, such as Poisson coefficient is negative, were nullified. ....	11
Figure 8 : Matrix and Fracture compressibility for dual-medium, function of skeleton shear and bulk moduli (top) and function of fracture porosity and shape factor (bottom). ....	12
Figure 9 : Drucker-Prager yield surfaces in the deviatoric plane and projection in $(-p',q)$ space with $p'$ = mean effective stress and $q$ = deviatoric stress.....	13
Figure 10 : Illustration of the toy model with the injection point at the left corner (equivalent to a quarter five-spot, with only one injection well). ....	14
Figure 11 : Cumulative surface displacement when considering Terzaghi formulation (red) or Biot formulation (green) for the simple medium case after one year of injection.....	15
Figure 12 : Evolution of the stress state from the initial state (left) to after one year of injection (right) in $(\Delta p, q)$ representation, for the Biot and Terzaghi approaches. Each point represents an element. If one of them cross the black line on the right ( $\Delta p = 0$ ), the failure criterion is reached. ....	16
Figure 13 : Cumulative surface displacement for the simple medium (red) or dual medium 1 (green) after one year of injection. ....	16
Figure 14 : Evolution of the stress state from the initial state (left) to after one year of injection (right) in $(\Delta p, q)$ representation, for the simple medium (SM) and dual medium (DM) cases. Each point represents an element. If one of them cross the black line on the right ( $\Delta p = 0$ ), the failure criterion is reached. ....	17
Figure 15 : Cumulative surface displacement for the dual medium 1 ( $\varphi_f=1e-5$ , red) or dual medium 2 ( $\varphi_f=1e-2$ , green) after one year of injection.....	17
Figure 16 : Evolution of the stress state from the initial state (left) to after one year of injection (right) in $(\Delta p, q)$ representation, for the dual medium 1 ( $\varphi_f=1e-5$ ) and 2 ( $\varphi_f=1e-2$ ) cases. Each point represents an element. If one of them cross the black line on the right ( $\Delta p = 0$ ), the failure criterion is reached. ....	18
Figure 17 : Differences in surface displacement between (Left) the dual medium 2 and dual medium 3a ( $k_f=30$ md,) and (Right) the dual medium 3a and dual medium 3b ( $k_f=300$ md) after one year of injection. ....	18
Figure 18 : Evolution of the stress state from the initial state (left) to after one year of injection (right) in $(\Delta p, q)$ representation, for the dual medium 2 ( $k_f=1e-10$ mD) and 3a ( $k_f=30$ mD) cases. Each point represents an element. If one of them cross the black line on the right ( $\Delta p = 0$ ), the failure criterion is reached. ....	19
Figure 19 : Evolution of the stress state from the initial state (left) to after one year of injection (right) in $(\Delta p, q)$ representation, for the dual medium 3a ( $k_f=30$ mD) and 3b ( $k_f=300$ mD) cases. Each point represents an element. If one of them cross the black line on the right ( $\Delta p = 0$ ), the failure criterion is reached. ....	19
Figure 20 : BHP and cumulative gas injection at surface conditions function of time for the different studied Dual-medium cases. ....	19
Figure 21 : Illustration of the synthetic model with the injection point at the left corner (equivalent to a quarter five-spot, with only one injection well) and with two facies: sandstone for the injection zone and the shallower aquifer/overburden (up-to the surface) and shale for the caprock and underburden. ....	21
Figure 22 : Initial conditions. From top to bottom: Total stress [MPa], Pressure [MPa] and Temperature [°C]. ....	21
Figure 23 : Temperature evolution [°C] at 0.5 year (left) and one year (right).....	22
Figure 24 : First seal rock element temperature evolution with time.....	23
Figure 25 : Comparison between isothermal and THM simulations results for the first seal rock element overpressure (top left), vertical effective stress (top right) and horizontal (bottom right) evolution with time. Bottom left: stress state projection in $(-p',q)$ for isothermal and THM simulations for the first seal rock element.....	23

## Earth Sciences and Environmental Technologies Division

Figure 26 : Vertical displacement [m] after one year of injection for the isothermal case (left) and THM case (right) [note: not the same color scale for both pictures].	24
Figure 27 : Comparison between isothermal and THM simulations results for the surface displacement (on top of the injection point).	24
Figure 28 : Presentation of the reference synthetic model.	25
Figure 29 : Zoom on the anticline and the sub-seismic fault, top reservoir layer.	26
Figure 30 : Geometric properties of the sub-seismic fault.	26
Figure 31 : Ground vertical displacement [m], at time $t=275$ days (i.e., phase 1, just before fracture opening) in the reference experiment. The green dashed line is a reference circle with a radius of 3200m.	28
Figure 32 : EW section of the vertical component of the ground surface displacement in meters, before fracture opening, in the reference experiment.	29
Figure 33 : Evolution of well pressure at the middle of the injection well, during the reference experiment.	29
Figure 34 : Pressure evolution through time inside the sub-seismic fault surface, in the reference experiment.	30
Figure 35 : Pressure evolution through time across the sub-seismic fault surface, in the reference experiment. The vertical and horizontal planes used for the visualization intersect each other along the injection well.	30
Figure 36 : Map of the total vertical displacement [m] of the ground surface. Left: during all the injection period. Right: during phase II. The green dashed line is the reference circle from Figure 31.	31
Figure 37 : EW cross-sections of the vertical ground surface displacement in the reference experiment. Left: during all the injection period. Right: during phase II.	31
Figure 38 : Ground surface displacement velocity along the EW profile at different times, in the reference experiment.	32
Figure 39 : EW vertical cross-section of the total displacement field in meters in the Z direction (Top) and X direction (Bottom), for all the injection period.	33
Figure 40 : EW cross-section of the total vertical displacement profiles of the reference experiment (curve with symbols) and of the same experiment but without fracture opening (curve without symbol) at $t=750$ days.	34
Figure 41 : Gas saturation inside the opened sub-seismic fault surface, at the end of the reference experiment.	34
Figure 42 : Gas saturation along 2 planes, horizontal and vertical, across the sub-seismic fault and along the injection well, at times $t=275$ days, $t=365$ days and $t=750$ days. Image on the right visualize the discretization and the position of the planes used for the visualization.	34
Figure 43 : EW vertical cross-section of the vertical ground displacement for 3 scenarii with varying fault lengths $L=8\text{km}$ (reference experiment), $L=3.3\text{km}$ and $L=2\text{km}$ .	35
Figure 44 : EW cross-section of the vertical ground displacement for two distances between the injector and the reservoir top, $L=100\text{m}$ and $L=25\text{m}$ .	36
Figure 45 : EW cross-section of the vertical ground displacement for 3 compressibility values of the overburden region of the sub-seismic fault: reference compressibility $C_p=1.e-3 \text{ bar}^{-1}$ , $C_p=1.e-4 \text{ bar}^{-1}$ , and $C_p=4.43 e-5 \text{ bar}^{-1}$ .	37
Figure 46 : EW cross-section of the vertical ground displacement at the end of 3 experiments: the reference one, an experiment with no sub-seismic fault opening and an experiment with sub-seismic fault opening as soon as injection starts.	38
Figure 47 : EW cross-section of the vertical ground displacement since fracture opening, for two experiments which differ in fault permeability increase at opening.	38
Figure 48 : Comparison of the vertical displacement pattern on the EW cross-section since the beginning of the injection for two experiments which differ in fault permeability increase at opening.	39
Figure 49 : EW cross-section of the vertical ground displacement for two experiments which differ in the caprock stiffness by a factor 10.	39
Figure 50 : From Rinaldi and Rutqvist, 2013. InSAR LOS displacement at In Salah injection site in the KB-502 well area.	45

## Annex B - Supplementary figures



**Fig. 8.** Comparison between simulated displacement and InSAR data. (a) Resulting displacement in the satellite line of sight. Black segment represents the KB-502 injection well. White, dashed segment represents the simulated fracture zone direction. Green and blue, dashed lines represent the direction of two profiles for the comparison with InSAR data at 500 m and 1700 m from the injection well, respectively. (b) InSAR data after 618 days of injection (23 December 2006). (c) Comparison between simulation (red line) and InSAR data (green, dashed line) along the profile 1 (500 m from the injection well). (d) Comparison between simulation (red line) and InSAR data (green, dashed line) along the profile 2 (1700 m from the injection well). InSAR data evaluated by MDA (MacDonald, Dettwiler and Associates Ltd.) Canada and Pinnacle Technology. (For interpretation of the references to color in this figure legend, the reader is referred to the web version of the article.)

**Figure 50 :** From Rinaldi and Rutqvist, 2013. InSAR LOS displacement at In Salah injection site in the KB-502 well area.